

TOO FAST FOR CHAOTIC, TOO SLOW FOR COHERENT: THE MISSING LINK BETWEEN ACCRETION, MASSIVE BLACK HOLE SPINS AND GALAXY KINEMATICS.

A. SESANA¹, E. BARAUSSE^{2,3}, M. DOTTI^{4,5}, E. M. ROSSI⁶

ABSTRACT

We present the results of a semianalytical model that evolves the masses and spins of massive black holes together with the properties of their host galaxies along the cosmic history. As a consistency check, our model broadly reproduces a number of observations, e.g. the cosmic star formation history, the black hole mass and luminosity function and the galaxy mass function at low redshift, the black hole to bulge mass relation, and the morphological distribution at low redshift. For the first time in a semianalytical investigation, we relax the simplifying assumptions of perfect coherency or perfect isotropy of the gas fueling the black holes. The dynamics of gas is instead linked to the morphological properties of the host galaxies, resulting in different spin distributions for black holes hosted in different galaxy types. We compare our results with the observed sample of spin measurements obtained through broad $K\alpha$ iron line fitting. The observational data disfavor both accretion along a fixed direction and isotropic fueling. Conversely, when the properties of the accretion flow are anchored to the kinematics of the host galaxy, we obtain a good match between theoretical expectations and observations. A mixture of coherent accretion and phases of activity in which the gas dynamics is similar to that of the stars in bulges (i.e., with a significant velocity dispersion superimposed to a net rotation) best describes the data, adding further evidence in support to the coevolution of massive black holes and their hosts.

Subject headings: black hole physics – accretion, accretion disks – galaxies: evolution – galaxies: kinematics and dynamics – galaxies: active – (galaxies:) quasars: supermassive black holes

1. INTRODUCTION

Observational evidence for the existence of massive black holes (MBHs) in the center of galaxies is circumstantial but convincing. Stellar orbits near the Galactic center point at the presence of a dark and massive object, which is too heavy and compact to be a cluster of low-luminosity bodies (Maoz 1998) or a fermion star (Schödel et al. 2002). Also, near-infrared observations of this object show that it is likely to have an event horizon, because if it did not, it would emit thermal radiation and be more luminous than observed (Broderick et al. 2009; Broderick & Narayan 2006). This disfavors exotic horizonless alternatives to General Relativity’s black holes, such as e.g. boson stars and gravastars. Similarly, MBHs are expected to be present in the center of most galaxies (and not just ours), as their presence is required to explain quasars (QSOs) and active galactic nuclei (AGNs) (Soltan 1982) and the cosmic downsizing (Scannapieco et al. 2005; Croton et al. 2006; Bower et al. 2006). Indeed, observations of nuclear stellar or gas dynamics, reverberation mapping, spectroscopic single epoch measurements and SED fitting (see e.g. Ghez et al. 2008; Gillessen et al. 2009; Kormendy & Richstone 1995; Miyoshi et al. 1995; Hicks & Malkan 2008; Blandford & Mc-

Kee 1982; Kaspi et al. 2005; Calderone et al. 2013; Castignani et al. 2013, and references therein for a discussion of the different methods) corroborate this expectation and allow the mass of the MBHs to be estimated. Furthermore, these MBH mass measurements have in turn resulted into the discovery of the MBH-galaxy relations (e.g. Gebhardt et al. 2000; Ferrarese & Merritt 2000; Marconi & Hunt 2003; Häring & Rix 2004a; Gültekin et al. 2009), hinting at a symbiotic evolution of the central compact object and its host galaxy.

MBHs are also expected to possess a spin angular momentum. The combination of mass and spin completely characterizes these objects if they are described by the black-hole solutions of General Relativity (Kerr 1963)⁷. If instead the gravity theory describing our Universe is not exactly given by General Relativity, other charges may be needed to describe MBHs, but the spin will still be one of them (c.f. Barausse & Sotiriou 2013; Yagi et al. 2012; Pani et al. 2011; Pani & Cardoso 2009, for a few examples of black holes in alternative gravity theories). Indeed, future spaced-based gravitational-wave interferometers such as ESA’s L3 experiment eLISA (Consortium et al. 2013) will measure MBH masses and spins with fantastic accuracy (respectively $\sim 0.1\%$ and $\sim 1\%$), and also put General Relativity to the test by e.g. measuring possible additional black-hole charges. More importantly from an astrophysical point of view, measurements of MBH spins could unveil still unknown links between the MBHs and their galactic hosts. As an example, knowledge of the spins could constrain the properties of the gas accreting onto the MBHs, e.g. whether it spirals toward it on a preferential plane, on completely isotropic directions, or with other more complex dy-

¹ Max Planck Institute for Gravitational Physics, Albert Einstein Institute, Am Mühlenberg 1, 14476, Golm, Germany
Email: alberto.sesana@aei.mpg.de

² CNRS, UMR 7095, Institut d’Astrophysique de Paris, 98bis Bd Arago, 75014 Paris, France
Email: barausse@iap.fr

³ Sorbonne Universités, UPMC Univ Paris 06, UMR 7095, 98bis Bd Arago, 75014 Paris, France

⁴ Dipartimento di Fisica G. Occhialini, Università degli Studi di Milano Bicocca, Piazza della Scienza 3, 20126 Milano, Italy
Email: massimo.dotti@mib.infn.it

⁵ INFN, Sezione di Milano-Bicocca, Piazza della Scienza 3, I-20126 Milano, Italy

⁶ Leiden Observatory, Leiden University, PO Box 9513 2300 RA Leiden, the Netherlands
Email: emr@strw.leidenuniv.nl

⁷ Black holes in General Relativity can also have an electric charge (Newman et al. 1965), but that is expected to be quickly canceled by the charges in the plasma surrounding astrophysical black holes, as well as by quantum effects such as Schwinger pair production (Gibbons 1975; Hanni 1982), or vacuum breakdown mechanisms triggering cascades of electron-positron pairs (Goldreich & Julian 1969; Ruderman & Sutherland 1975; Blandford & Znajek 1977).

namics (Dotti et al. 2013).

Until eLISA or a similar space-based gravitational-wave interferometer is launched, however, measuring the spins of MBHs is considerably more difficult than measuring their masses. This is because the spin affects the dynamics of stars and gas surrounding the MBH only at distances orders of magnitudes smaller than the MBH influence radius (e.g. Bardeen & Petterson 1975). Currently, the most accurate way of measuring the spins of MBHs is through the spectra of relativistically broadened $K\alpha$ iron lines (see Reynolds 2013; Brenneman 2013, for recent reviews on the topic). Indeed, using current X-ray spectrographs (in particular XMM and Suzaku), a significant sample of MBHs with spin estimates is being built up. Also, more stringent constraints on the spin estimates are becoming available from hard X-ray data from NuSTAR (Risaliti et al. 2013). Finally, spin measurements with $K\alpha$ iron lines are one of the main scientific drivers of ESA's upcoming L2 mission ATHENA+ (Nandra et al. 2013).

This situation clearly calls for a theoretical framework capable of interpreting the already available data for MBH spins and making testable predictions for future measurements. However, detailed modeling of the MBH spin evolution is still missing. Since the spin is a vector, any theoretical model should take the evolution of the spin direction into account, because that also affects the evolution of the magnitude. This is particularly clear when one considers MBH mergers, which are expected in the late stages of galaxy mergers (e.g. Begelman et al. 1980). Indeed, the final spin, mass and kick velocity of the MBH remnant resulting from such mergers critically depend on the orientations of the spins of the progenitors, and this dependence was studied in detail using numerical and semi-analytical techniques (Rezzolla et al. 2008; Barausse & Rezzolla 2009; Buonanno et al. 2008; Barausse et al. 2012; Lousto & Zlochower 2009; van Meter et al. 2010).

The main driver of the MBH evolution, however, is not expected to be given by mergers but rather by radiative efficient gas accretion (Soltan 1982; Merloni et al. 2004; Shankar et al. 2004). In this case, the spin magnitude evolution depends on whether the gas in the very central regions of the accretion disk is co-rotating or counter-rotating relative to the MBH spin. This in turn depends on the larger-scale properties of the fueling process (i.e. if the gas keeps on falling toward the MBH on some preferential plane), as well as on the possible re-alignment of the MBH-disk system due to the Bardeen-Petterson effect (Bardeen & Petterson 1975), i.e. the interplay between the frame dragging from the rotating spacetime geometry and the viscous stresses in the disk. However, the details of the effect of the spacetime's geometry on the properties of accretion disks are still not completely understood (see, e.g. Sorathia et al. 2013b,a, and references therein). All the studies that follow the coupled evolution of the magnitude and direction of the MBH spin have been performed under some simplifying hypotheses: i.e. assuming that the disk has isotropic viscosity (see the discussion in Sorathia et al. 2013b,a), using order of magnitude estimates for the effect of the alignment (e.g. King & Pringle 2006), or under the small-deformation approximation for the warped disk (e.g. Perego et al. 2009).

These simplifying hypotheses allowed for simple recipes for the spin evolution that have been used in semi-analytical models of structure formation and evolution (see, e.g. Volonteri et al. 2005; Berti & Volonteri 2008; Lagos et al. 2009; Fanidakis et al. 2011, 2012; Barausse 2012; Volonteri et al. 2007, 2013). However, most of these studies (Volonteri et al.

2005; Berti & Volonteri 2008; Lagos et al. 2009; Fanidakis et al. 2011, 2012) assume that the MBH fueling is either always coherent (i.e. accretion always occurs exactly on the equatorial plane), or statistically isotropic (i.e. the MBH accretes small gas clouds with randomly oriented angular momenta). These assumptions were partly relaxed in Barausse (2012); Volonteri et al. (2007, 2013), who noted that the Bardeen-Petterson effect is likely to align the MBH spin with the angular momentum of the accreting gas in gas-rich nuclear environments, thus making the accretion flow effectively coherent in such situations, as opposed to isotropic accretion, which is more likely in gas-poor nuclear environments. Even with this improvement, however, the possible parameter space of the accretion flow is still limited to two points (coherent accretion in gas-rich environments vs isotropic one in gas-poor environments).

Recently Dotti et al. (2013) demonstrated that the spin evolution can indeed be significantly different if a more realistic description of the accretion flow is adopted, namely one that allows regimes intermediate between the perfectly coherent and perfectly isotropic cases mentioned above. Dubois et al. (2013) studied the evolution of the spins of a population of MBHs taking into consideration the dynamical properties of the fueling gas. They extracted the direction of the angular momentum of the accreting matter on the smallest scales resolved by hydrodynamical simulations (down to ≈ 10 pc in their highest resolution run). In a similar spirit, in this paper we couple the semianalytic model of Barausse (2012) to the spin evolution model of Dotti et al. (2013) by linking the characteristics of the accretion flow (and in particular its degree of coherence/isotropy) to the observed properties of the host galaxy, and in particular to the dynamical parameters of the gas and stars observed in galactic nuclei. We stress that, also in our case, most of the observations that we use have a spatial resolution $\gtrsim 100$ pc, significantly larger than the typical accretion disk scales, and that the dynamical properties of the gas could change at smaller unresolved scales (e.g. Hopkins et al. 2012; Maio et al. 2013; Dubois et al. 2014). In this sense, therefore, a comparison of the predictions of our model for the MBH spins with actual spin measurements provides a way of testing the dynamics and coherence of the nuclear gas at yet unresolved scales. We attempt such a test with the MBH spin measurements from $K\alpha$ iron lines available to date. We stress, however, that our model provides a flexible framework to interpret also future more accurate measurements from experiments such as eLISA and ATHENA+.

The paper is organized as follows. In section 2 we present the details of our model for the evolution of MBHs in their galactic hosts. As mentioned above, the model is based on that of Barausse (2012), with a few improvements in the star-formation law (section 2.1), and more importantly in the prescription for the evolution of the MBH spins under accretion, which we adapt from Dotti et al. (2013) and which we present in section 2.2. The one unknown in our model is the degree of coherence of the accretion flow, but in section 2.3 we show how to link it to the kinematic properties of the host galaxy. We consider in particular two models, one where the degree of coherence is related to the gas kinematics, and one that links it to the stellar kinematics. In section 3 we present our predictions for the evolution of the MBH spins in either model, and in 4 we compare them to the available measurements of MBH spins obtained via $K\alpha$ iron lines. In section 5 we draw our conclusions.

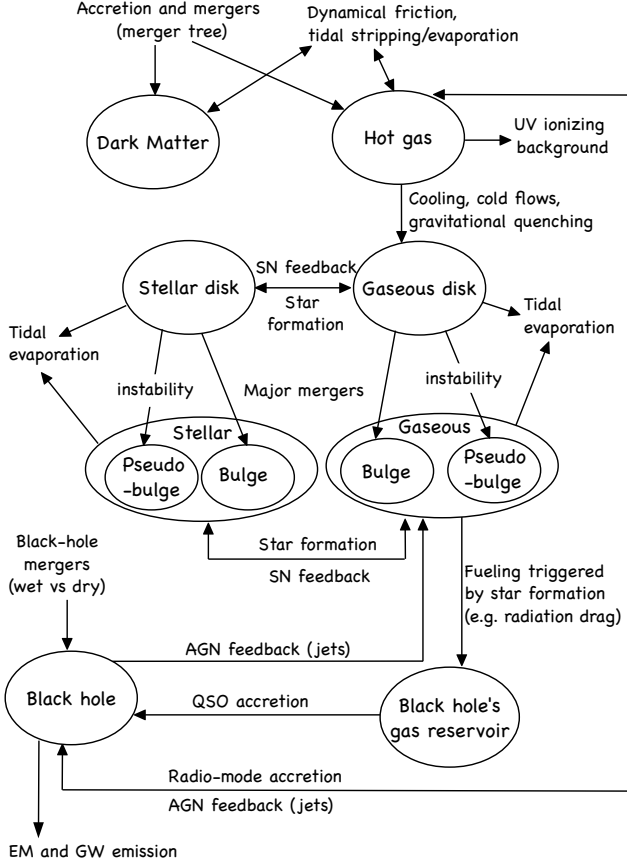


FIG. 1.— Schematic representation of our semianalytical model, based on that of B12. Note that B12 did not use the distinction between “bulges” forming from major galactic mergers and “pseudobulges” forming from bar-instabilities of disk galaxies (although both formation channels were present). In this paper, instead, we assume that bulges and pseudobulges have different star-formation laws (c.f. sec. 2.1) and, in some realizations of our model, different accretion properties onto the central MBH (c.f. 2.3). The other major change from the model of B12 is indeed the prescription for the spin evolution of MBHs under accretion and mergers, which is schematically represented in Figure 2 and described in detail in sec. 2.2.

2. THE MODEL

The model presented in this paper is based on that of Barausse (2012), hereinafter B12, who studied the symbiotic co-evolution of MBHs (and in particular of their spins) with their host galaxies, using a state-of-the-art semianalytical galaxy-formation model. More specifically, B12 describes the Dark-Matter evolution by merger trees produced with the extended Press-Schechter formalism and suitably modified to reproduce the results of N-body Dark-Matter simulations (Cole et al. 2008). The baryonic content of galaxies is evolved along the branches of the merger tree and includes several components, namely a hot-gas phase, a cold-gas disk, a stellar disk, a cold-gas bulge, a stellar bulge, a MBH and a reservoir of cold gas fueling accretion onto the MBH. Gravitational interactions among the various components are accounted for (although in simplified ways), which allows for calculating reasonable estimates for the density and velocity fields of each component. Also modeled are a variety of non-gravitational interactions, which are summarized schematically in Figure 1. We refer the reader to B12 for more details, and focus here only on some later improvements that we made on the model. More specifically, in section 2.1 we describe an improved star-formation implementation, which is based on Krumholz et al.

(2009) and which produces predictions in better agreement with observations (c.f. Figure 9). Also, in this new star-formation prescription, we will attempt to discriminate the bulge component into classical bulges – resulting from major galactic mergers and giving bursts of star formation –, and pseudobulges – resulting from bar-instabilities of disk galaxies and undergoing a more quiescent, disk-like star formation (see, e.g. Kormendy 2013). While both bar-instabilities and major mergers were modeled in B12, the distinction between bulges and pseudobulges was not present in that paper, in the sense that the bulge component would behave in the same manner irrespective of its formation mechanism. In section 2.2 we will instead describe how the spin evolution under accretion and mergers is followed in our model. Our implementation is largely based on the proposal of Dotti et al. (2013), thus improving on the original model of B12, which, as we will explain, is similar to that of Dotti et al. (2013) in a particular limit, namely when the “isotropy” parameter F is exactly $1/2$ (i.e. when gas is accreted isotropically onto the MBH). Unlike Dotti et al. (2013), however, here we will not treat F as a free parameter, but rather attempt to relate it to the kinematic properties of galaxies, i.e. to the velocity dispersion of stars and gas resulting from the different galactic morphologies, as detailed in section 2.3.

2.1. The star formation

Our prescription for the star formation law is based on the work by Krumholz et al. (2009), extended to include the low metallicity (less than 1% solar, Krumholz & Gnedin 2011; Krumholz 2012; Forbes et al. 2013; Kuhlen et al. 2013) and starburst regimes (Daddi et al. 2010; Genzel et al. 2010). The advantage with respect to the implementation of B12 is that the star formation is an explicit function of metallicity, which allows for better modeling of the building up of stars in different galaxies, at various redshifts and environments.

Observations of our and nearby galaxies have established that star formation is ultimately associated with Giant Molecular Clouds (GMCs), *giant* because they can be very massive ($M \sim 10^6 M_\odot$) and extended (~ 100 pc). There, the star formation rate is determined by the mass fraction f_c in cold gas (generally, but not only, in molecular form) and the timescale t_{SF} needed to convert it into stars. This latter depends both on the cloud properties, such as its density (the higher the faster is the process) and on the presence of feedback-driven turbulence, which slows the collapse. One of the main (observationally supported) assumptions is that the GMC properties are environment independent, until the surrounding interstellar medium has lower pressure than the GMC itself. In particular, the cloud surface density Σ_{cl} is set by internal processes to be always around $\Sigma_{\text{cl}} \approx 85 M_\odot \text{ pc}^{-2}$ in more tenuous environments, where the gas surface density is $\Sigma_g \leq 85 M_\odot \text{ yr}^{-1} \equiv \Sigma_{\text{th}}$ (e.g. Bolatto et al. 2011). Above this threshold, pressure equilibrium between the interstellar medium and the GMC sets $\Sigma_{\text{cl}} \simeq \Sigma_g$.

2.1.1. Star formation in the galactic disk

In this framework, the local star formation in the galactic disk can be described by

$$\dot{\Sigma}_* = \frac{f_c \Sigma_g}{t_{\text{SF}}}, \quad (1)$$

where the timescale t_{SF} has two regimes, according to whether the cloud density Σ_{cl} is set by the interstellar pres-

sure,

$$t_{\text{SF}}^{-1} = \frac{M_6^{-0.33}}{0.8 \text{ Gyr}} \max \left[1, \left(\frac{\Sigma_g}{\Sigma_{\text{th}}} \right)^{0.67} \right], \quad (2)$$

(Krumholz et al. 2009), where $M_6 = M/(10^6 M_\odot)$ is the GMC mass. The local Jeans mass $M_j \approx \sigma_g^2/G^2 \Sigma_g$ gives a good estimate of the cloud mass, where σ_g is the gas velocity dispersion. In a galactic *disk* environment, we may assume a condition of marginal gravitational stability, and obtain a function of the background gas surface density only,

$$t_{\text{SF}}^{-1} = (2.6 \text{ Gyr})^{-1} \times \begin{cases} \left(\frac{\Sigma_g}{\Sigma_{\text{th}}} \right)^{-0.33}, & \Sigma_g < \Sigma_{\text{th}}, \\ \left(\frac{\Sigma_g}{\Sigma_{\text{th}}} \right)^{0.34}, & \Sigma_g > \Sigma_{\text{th}}. \end{cases} \quad (3)$$

The cold-gas mass fraction f_c is equivalent to the molecular mass fraction at metallicity greater than $\sim 1\%$ solar, when H_2 has time to form before collapsing and forming stars. At lower metallicities, instead, star formation will occur in a cold atomic gas phase rather than a molecular phase (Krumholz 2012). In general, as the metallicity decreases, the cold gas available for forming stars decreases as well. However, recent observations of nearby spirals and dwarfs (Bigiel et al. 2010) and of the Small Magellanic Cloud (Bolatto et al. 2011) suggest that f_c levels off, around 2% rather than dropping to zero. These considerations let us adopt the following prescription,

$$f_c = \begin{cases} 1 - \left[1 + \left(\frac{3}{4} \frac{s}{1+\delta} \right)^{-5} \right]^{-1/5}, & \text{if } f_c > 2\%, \\ 2\%, & \text{otherwise.} \end{cases} \quad (4)$$

(Krumholz private communication), with

$$s = \ln(1 + 0.6\chi)/(0.04\Sigma_1 Z'),$$

$$\chi = 0.77(1 + 3.1Z'^{0.365}),$$

$$\delta = 0.0712(0.1s^{-1} + 0.675)^{-2.8},$$

where $\Sigma_1 = \Sigma_g/(M_\odot \text{ pc}^{-2})$ and Z' is the metallicity in Solar units.

Integrating equation (1) over the entire disk surface, we obtain the total star formation rate in the disk.

2.1.2. Star formation in the galactic bulges

The very same prescription can be applied to the bulge, during the periods of “quiescent star-formation” in the galaxy, i.e. when violent star bursting events are not triggered. Practically, we use a volumetric star formation law,

$$\dot{\rho}_* = \frac{f_c \rho_g}{t_{\text{SF}}}, \quad (5)$$

which we derive directly from equation (1), by expressing Σ_g and M as a function of the volumetric gas density ρ_g and the local isothermal sound speed c_s .

Let us start by considering the star formation timescale (equation (2)). In regions with densities below threshold, $t_{\text{SF}} \propto M_j^{0.33}$, where we can simply write the Jeans mass in the more familiar way

$$M_j = \frac{\pi}{6} \frac{c_s^3}{G^{3/2} \rho_g^{1/2}} \approx 10^6 M_\odot \left(\frac{c_s}{8.3 \text{ km/s}} \right)^3 \rho_1^{-1/2}, \quad (6)$$

with $\rho_1 = \rho_g/(M_\odot/\text{pc}^3)$. In denser regions of the bulge, one has an additional dependence on Σ_{cl} , i.e. $t_{\text{SF}} \propto M_j^{0.33} \Sigma_{\text{cl}}^{-0.67}$ (c.f. equation (2)). To relate the surface density to the volume density, let us note that for a spherical cloud of mass M and characteristic size L , $\rho_{\text{cl}} \approx M/L^3$ and $L \approx \Sigma_{\text{cl}}/\rho_{\text{cl}}$. Eliminating L in these two expressions, we obtain $\rho_{\text{cl}} \approx M_\odot \text{ pc}^{-3} (\Sigma_{\text{cl}}/\Sigma_{\text{th}})^{3/2} M_6^{-1/2}$. Inserting equation (6) and recalling the pressure equilibrium condition, $\rho_g \approx \rho_{\text{cl}}$ (Krumholz & McKee 2005), we finally get

$$\left(\frac{\Sigma_g}{\Sigma_{\text{th}}} \right) = \rho_1^{1/2} \left(\frac{c_s}{8.3 \text{ km/s}} \right). \quad (7)$$

Thus, the overall timescale expression becomes

$$t_{\text{SF}}^{-1} = (0.8 \text{ Gyr})^{-1} \times \begin{cases} \rho_1^{0.165} \left(\frac{c_s}{8.3 \text{ km/s}} \right)^{-0.99} & \Sigma_g < \Sigma_{\text{th}}, \\ \rho_1^{1/2} \left(\frac{c_s}{8.3 \text{ km/s}} \right)^{-0.32} & \Sigma_g > \Sigma_{\text{th}}. \end{cases} \quad (8)$$

We now turn our attention to the fraction of mass in cold gas available for star formation, f_c (equation (4)). Unlike, t_{SF} , it depends on the *gas* density and *not* on the GMC density. In more tenuous regions, out of pressure equilibrium, the cloud can be denser than the background gas, $\eta \equiv \rho_{\text{cl}}/\rho_g \geq 1$. Therefore, in principle, we should use a modified equation (7), $\Sigma_g \propto \eta^{-1/3} \rho_g^{1/2} c_s$, which allows us to use this expression both above ($\eta \approx 1$) and *below* threshold. However, since f_c has a floor of 2% (c.f. equation (4)), which kicks in when $\eta \approx$ a few to several, the modification factor ($\eta^{-1/3} \approx 1 - 2$) is negligible relative to the other uncertainties in the derivation of equation (7). We will therefore always use directly equation (7) into equation (4), whether above or below threshold.

2.1.3. Starburst in Merging Galaxies

Observations suggest a link between starbursts and mergers. The main evidence is that the strongest starbursts (Ultra- and Hyper-Luminous Infrared Galaxies) are predominantly merging systems at all redshifts (e.g. Elbaz & Cesarsky 2003). More recently, CO observations of galaxy populations hinted that starburst/merging galaxies have a different, more efficient, star formation law (Daddi et al. 2010; Genzel et al. 2010). We therefore assume that in merging systems the star formation is driven by different dynamical processes in the bulge, which induce star formation over a dynamical time. In practice, we use the same procedure as in B12: in the gaseous bulge that forms after the merger, star formation is regulated by

$$\dot{\rho}_* = \frac{\rho_g}{t_{\text{ff}}}, \quad (9)$$

where $t_{\text{ff}} = \sqrt{3\pi/(32G\rho_g)}$ is the local dynamical time for the gas. Again, this expression can be integrated over the bulge volume to yield the total star formation rate.

2.2. The spin evolution

Two main processes drive the cosmic evolution of MBH spins: accretion of gas from the inter-stellar medium (ISM) and inter-galactic medium (IGM), and mergers between MBHs. In this section we will shortly summarize the main aspects of the implementation of these two channels, focusing on the main improvements with respect to B12. The model we adopt in this paper is summarized schematically in Figure 2.

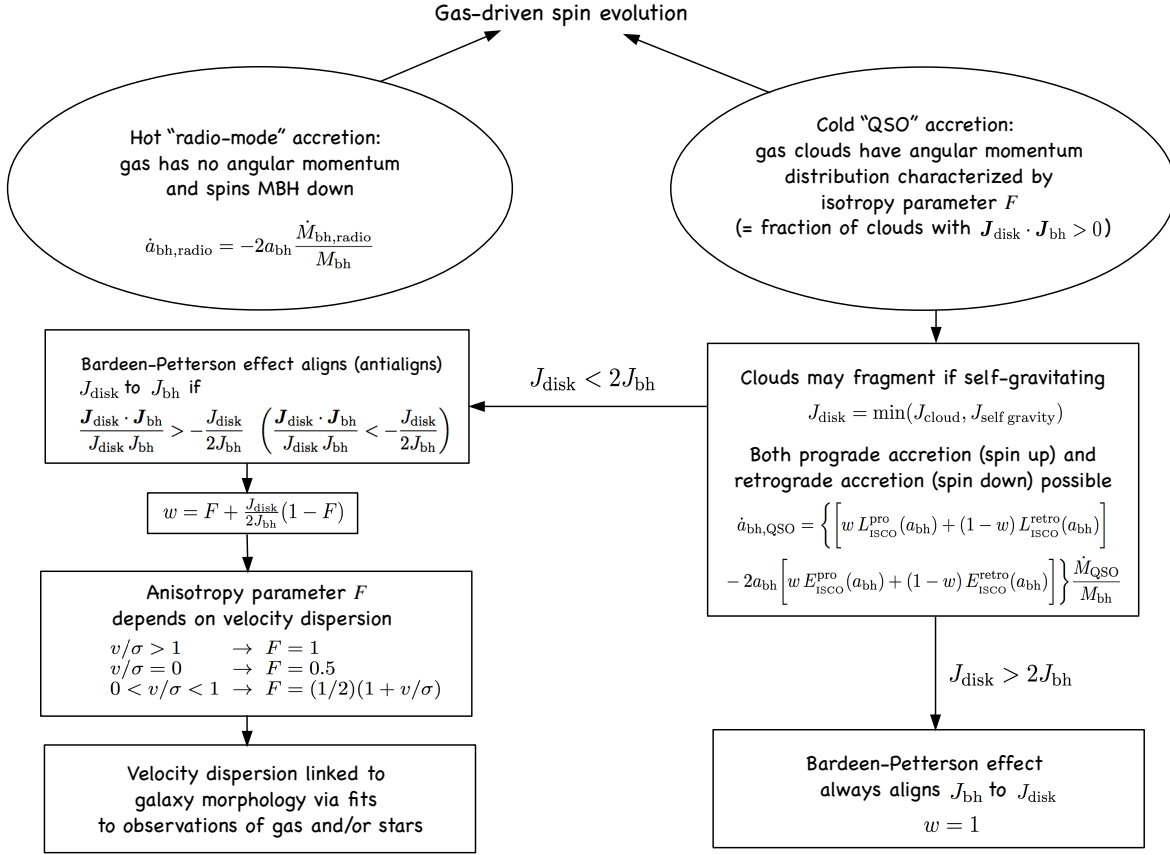


FIG. 2.— Scheme of the possible accretion driven MBH spin evolution channels.

We will start with the discussion of gas accretion, which is believed to be the main driver of the MBH spin evolution (Berti & Volonteri 2008, B12), with the possible exception of the most massive black holes in massive, gas-poor, low-redshift ellipticals (e.g., Fanidakis et al. 2011). Because of the vectorial nature of the spin, its evolution depends on the dynamical properties of the accreting gas, in particular on the distribution of the angular momentum magnitude and direction of the accreting clouds. For this reason, we identify different spin evolution channels, as detailed below and summarized in Figure 2. Following B12 we distinguish two main modes of gas accretion:

- a hot “radio” mode when the MBH accretes IGM gas that cools on a timescale longer than its free fall time. In this regime the gas is approximately spherically symmetric, so no net angular momentum is acquired by the MBH and the spin parameter a_{bh} changes (to first approximation) only because of the increase of the MBH mass:

$$\dot{a}_{\text{bh,radio}} = -2a_{\text{bh}} \frac{\dot{M}_{\text{bh,radio}}}{M_{\text{bh}}}, \quad (10)$$

where $\dot{M}_{\text{bh,radio}}$ is the Bondi accretion rate of the hot IGM component (see equation (44) in B12). This mode has a negligible direct impact on the mass and spin evolution of MBHs, because it is typically characterized by very low accretion rates, but plays a major role in activating jets capable of exerting an “AGN feedback” on the growth of large cosmic struc-

tures (B12).

- A cold “QSO” mode correlated with star formation in the bulge, which is supposed to drive cold ISM gas into a low-angular momentum reservoir with mass M_{res} available for accretion onto the MBH. Star formation events in the bulge are caused, in the framework of B12, by major mergers or by bar instabilities of gaseous galactic disks. As mentioned in sec. 2.1, here we discriminate between quiescent star-formation activity in “pseudobulges” forming from disk instabilities, and more violent starbursts in bulges forming from major mergers. Following B12 (see also Granato et al. 2004; Haiman et al. 2004), we assume that the influx of gas into the reservoir is correlated with bulge star formation. As a result, major mergers tend to produce larger reservoirs and MBH accretion rates than disk instabilities. Once the cold gas has settled in the reservoir, we follow Granato et al. (2004) and assume that it accretes onto the MBH with instantaneous rate

$$\dot{M}_{\text{QSO}} = \min(\dot{M}_{\text{visc}}, A_{\text{Edd}} \dot{M}_{\text{Edd}}). \quad (11)$$

Here, $\dot{M}_{\text{visc}} = k_{\text{accr}} \sigma^3 M_{\text{res}} / (GM_{\text{bh}})$ (Granato et al. 2004; Granato private communication) is the viscous accretion rate, where we set⁸ $k_{\text{accr}} = 10^{-3}$ and $\sigma = 0.65 V_{\text{vir}}$ (V_{vir} being the halo’s virial velocity); \dot{M}_{Edd} is the Eddington mass accretion rate (related to the Eddington luminosity L_{Edd} by $\dot{M}_{\text{Edd}} =$

⁸ Note that k_{accr} is related to the critical Reynolds number $\mathcal{R}_{\text{crit}}$ for the onset of turbulence by $k_{\text{accr}} = 1/\mathcal{R}_{\text{crit}}$.

$L_{\text{Edd}}/[\eta(a_{\text{bh}})c^2]$, $\eta(a_{\text{bh}})$ being the accretion electromagnetic efficiency, which is a function of the spin a_{bh} and the fraction of prograde vs retrograde accretion events, c.f. equation (13)); and $A_{\text{Edd}} \geq 1$ is a free parameter regulating the amount of super-Eddington accretion allowed in our model. We stress that this prescription for \dot{M}_{QSO} replaces the simpler recipe of B12, which assumed $\dot{M}_{\text{QSO}} = M_{\text{res}}/t_{\text{accr}}$, with t_{accr} a free parameter on the order of 5×10^8 yr.

Another difference with respect to B12 consists in the way we estimate the amount of matter M_{disk} captured by the MBH during each single accretion episode of the cold gas stored in the reservoir. Here, we follow the model of Dotti et al. (2013), and take M_{disk} to be the minimum between a free parameter M_{cloud} – which we set to $3 \times 10^4 M_{\odot}$ and defines the characteristic mass of each lump of matter infalling toward the MBH – and the mass M_{sg} of a disk truncated at the self-gravity radius, where the Toomre parameter reaches a value of $Q = 1$. This is because outside this radius, the accretion disk that forms from the infalling cloud will fragment under its self gravity and be consumed by star formation (see Perego et al. 2009; Dotti et al. 2013, for details).

Gas accreting in the QSO mode is assumed to settle in a standard thin accretion disk with a non-zero angular momentum. In this scenario the spin evolves as

$$\dot{a}_{\text{bh,QSO}} = \left\{ \left[w L_{\text{ISCO}}^{\text{pro}}(a_{\text{bh}}) + (1-w) L_{\text{ISCO}}^{\text{retro}}(a_{\text{bh}}) \right] - 2a_{\text{bh}} \left[w E_{\text{ISCO}}^{\text{pro}}(a_{\text{bh}}) + (1-w) E_{\text{ISCO}}^{\text{retro}}(a_{\text{bh}}) \right] \right\} \frac{\dot{M}_{\text{QSO}}}{M_{\text{bh}}}, \quad (12)$$

where $L_{\text{ISCO}}^{\text{pro}}(a_{\text{bh}})$ and $E_{\text{ISCO}}^{\text{pro}}(a_{\text{bh}})$ are respectively the specific angular momentum and specific energy at the prograde innermost stable circular orbit (ISCO), $L_{\text{ISCO}}^{\text{retro}}(a_{\text{bh}})$ and $E_{\text{ISCO}}^{\text{retro}}(a_{\text{bh}})$ are the same quantities for the retrograde ISCO, and w is the fraction of rest mass that accretes on prograde orbits. Likewise, the accretion efficiency is calculated by weighing the prograde and retrograde thin-disk efficiencies $\eta_{\text{pro}}(a_{\text{bh}})$ and $\eta_{\text{retro}}(a_{\text{bh}})$:

$$\eta(a_{\text{bh}}) = w\eta_{\text{pro}}(a_{\text{bh}}) + (1-w)\eta_{\text{retro}}(a_{\text{bh}}). \quad (13)$$

The fraction w of prograde accretion is given by

$$w = 1 \quad \text{if } J_{\text{disk}} > 2J_{\text{bh}} \\ w = F + \frac{J_{\text{disk}}}{2J_{\text{bh}}}(1-F) \quad \text{if } J_{\text{disk}} < 2J_{\text{bh}}. \quad (14)$$

Here, J_{disk} is the angular momentum of the single lump of matter accreting onto the MBH, and is obtained from the lump’s mass, $M_{\text{disk}} = \min(M_{\text{cloud}}, M_{\text{sg}})$, using equations (2) and (6) of Dotti et al. (2013) and equation (11) of Perego et al. (2009). Also, F measures the probability that the lump’s angular momentum is initially tilted by an angle $\theta_{\text{out}} < \pi/2$ relative to the MBH’s spin, i.e. F is an “isotropy parameter” measuring the fraction of accretion events with angular momentum initially pointing in the MBH’s “northern hemisphere” (c.f. Dotti et al. (2013) for more details).

The relation between F and w encoded in equation (14) is given by the Bardeen Petterson effect (Bardeen & Petterson 1975). More specifically, when $J_{\text{disk}} > 2J_{\text{bh}}$, the MBH spin aligns with the angular momentum of the outer regions of the accretion disk that forms when the lump of matter falls into the MBH, and the alignment happens on a timescale smaller than the accretion timescale. Most of the accreted gas then has

angular momentum aligned with the MBH spin, hence $w = 1$ and the MBH spins up. In this limiting case, equation (12) tends to equation (38) of B12. If instead $J_{\text{disk}} < 2J_{\text{bh}}$, King et al. (2005); King & Pringle (2006) showed that on a similarly short timescale, the inner accretion flow’s angular momentum *antialigns* with the MBH spin if the angle between the outer disk’s angular momentum and the MBH spin satisfies $\theta_{\text{out}} > \pi/2$ and $\cos \theta_{\text{out}} < -J_{\text{disk}}/(2J_{\text{bh}})$. Assuming that the fraction $1 - F$ of accretion events with $\theta_{\text{out}} > \pi/2$ is distributed isotropically, one then obtains the second expression for w in equation (14).

Let us note that in the limit of $J_{\text{disk}}/2J_{\text{bh}} \ll 1$ (always valid for very massive MBHs, $M_{\text{bh}} \gtrsim 10^9 M_{\odot}$), our model becomes very simple, as it predicts that the MBHs will move toward an equilibrium spin parameter a_{eq} function of F , obtained by setting $\dot{a}_{\text{bh,QSO}} = 0$ in equation (12), after substituting w with F by equation (14). The value of a_{eq} as a function of F is shown in Figure 3.

We should stress, however, that equation (14) *i)* only provides an “averaged” version of the stochastic scenario proposed by Dotti et al. (2013) (i.e. our prescription does not follow each individual accretion event, but only approximates the model of Dotti et al. (2013) over many such events), and *ii)* does not take into account the detailed evolution of the accretion disk during the (short) alignment process (the details of the alignment mechanism are, in any case, still under debate, see e.g. Sorathia et al. 2013b,a, and references therein). A more accurate treatment of the spin evolution addressing these two shortfalls is beyond the scope of the paper, but we expect the impact of these simplifications on the spin evolution to be small. Regarding *i)*, the mass M_{res} of the reservoir available for accretion onto the MBH is typically much larger than M_{disk} (thus averaging out the stochastic character of the model of Dotti et al. 2013), except in the “tails” of the accretion process (i.e., when M_{res} is small before and after a QSO event), when accretion rates (and thus the changes in the spin) are in any case small. We have indeed tested that replacing $M_{\text{cloud}} \rightarrow \min(M_{\text{res}}, M_{\text{cloud}})$, which corresponds to changing our model’s prescription in the tails of the accretion process, does not alter our results significantly. As for *ii)*, our neglecting the short alignment process is typically justified, as the alignment takes place on timescales shorter than accretion. Nevertheless, even a small amount of retrograde accretion during the alignment can potentially lower the spin significantly near the $a_{\text{bh}} = 1$ limit, and we will return to this point in section 4.3.

The fraction F was left as a free parameter in Dotti et al. (2013), while B12 adopted a model similar to (although more simplistic than) the one described above, but assuming $F = 0.5$ for every MBH (see equation (39) in B12). This implicitly assumes that the material infalling toward the central MBH has, on average, no net angular momentum, i.e. no preferential orbital plane. Here we attempt to link F to the dynamical properties of the host galaxies, and in particular to the v/σ ratio, where v is the bulk rotation velocity of the system and σ is its velocity dispersion (measuring how “chaotic”, in an astrophysical sense, the system is). In sec. 2.3 we discuss the various measurements of v/σ in galactic nuclei (as close as possible to the MBH) that we will use in this paper.

The relation between v/σ and F can be derived as follows. Suppose that the net rotation is along the z axis. Each lump of matter falling into the MBH has an angular momentum with z -component $L_z = mr \sin \theta (v + \sigma_{\varphi})$, where θ and φ are the

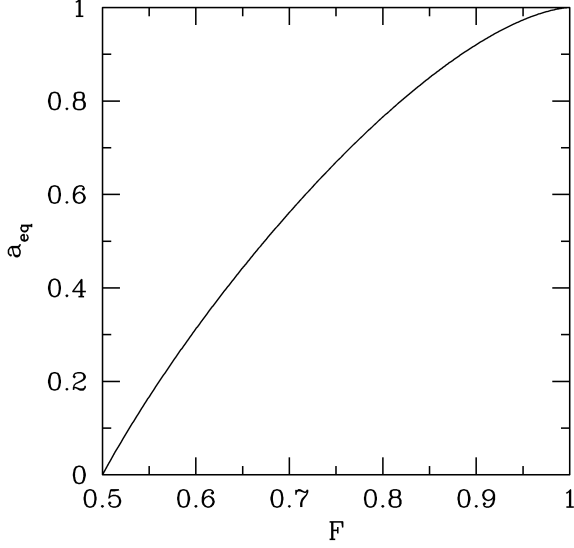


FIG. 3.— Equilibrium spin parameter as a function of the “isotropy parameter” F . Here we assume that each single accretion episode has a very small angular momentum compared to the MBH, so that both alignment and counteralignment can occur (see text for details).

polar and azimuthal angles in a spherical coordinate system, and σ_φ is the projection of σ on the tangential direction e_φ . Let us now write $\sigma_\varphi = \sigma \cos \alpha$, where α is the angle between σ and e_φ . If σ is isotropically distributed, $\cos \alpha$ has a uniform probability distribution, i.e. $dP/d\cos \alpha = 1/2$. If $v/\sigma > 1$, L_z is always positive and $F = 1$. If $0 \leq v/\sigma < 1$, the probability of having $L_z > 0$ (or $L_z < 0$) is proportional to $1 + v/\sigma$ (or $1 - v/\sigma$), hence $F = (1 + v/\sigma)/2$. In summary, we assume

$$\begin{aligned} v/\sigma > 1 &\rightarrow F = 1; \\ v/\sigma = 0 &\rightarrow F = 0.5; \\ 0 < v/\sigma < 1 &\rightarrow F = (1 + v/\sigma)/2. \end{aligned} \quad (15)$$

We stress that our implementation implicitly assumes that at the beginning of each accretion event the MBH spin is exactly aligned with the total angular momentum of the gas reservoir, i.e. with the average angular momentum of the clouds. This is not the case under many circumstances. Suppose again that the net rotation is along the z axis, and that the MBH is light enough to be in the $J_{\text{disk}}/2J_{\text{bh}} > 1$ regime. When a new cloud is accreted, the spin of the MBH is initially aligned with the angular momentum direction of the latest accreted cloud, which will differ from z whenever a minimum degree of turbulence/anisotropy is present in the fueling material. Still, assuming the MBH spin to be aligned with z does not affect significantly the evolution of the spin magnitude of MBHs with $M_{\text{bh}} \lesssim 10^7 M_\odot$, since the MBH spin immediately realigns with the disk’s angular momentum in the $J_{\text{disk}}/2J_{\text{bh}} > 1$ regime. The high mass regime of our model is instead exact for the two limiting cases $F = 0.5$ and $F = 1$, and it also preserves the correct monotonic trend of higher a_{bh} for higher values of F . It is possible to estimate the effect of the initial MBH orientation for $0.5 < F < 1$ by comparing Figure 3 with the results for $M_{\text{bh}} \gtrsim 10^9 M_\odot$ in (Dotti et al. 2013). We postpone a more detailed analysis to future work.

Finally, our prescription of the MBH mergers closely follows that of B12, to which we refer the reader for more details. In summary, we use the phenomenological formulas of

Barausse & Rezzolla (2009) and van Meter et al. (2010) to predict the final spin and recoil velocity of the MBH resulting from the merger, and check whether the recoil ejects the MBH from the galaxy. For the mass of the MBH produced by the merger, we update the prescription of B12 by adopting the phenomenological formula of Barausse et al. (2012). We stress that these formulas produce results in accurate agreement with fully general-relativistic simulations. The only other change from the implementation of B12 regards the criterion to discriminate “wet” mergers (where the MBH spins are aligned by the circumbinary disk via the Bardeen-Petterson effect), from “dry” mergers, where such alignment does not take place and the spins are isotropically distributed. Improving on B12, who compared M_{res} to the mass of the MBH binary to distinguish the two regimes, here we assume that a merger happens with aligned spins if $J_{\text{res}} > 2(S_1 + S_2)$ (where J_{res} is the angular momentum of the cold gas reservoir, and $S_{1,2}$ are the spins of the two MBHs), while otherwise we assume that the spins are randomly oriented. This prescription is preferable to that of B12, because the Bardeen-Petterson effect is sensitive to the angular momenta of the circumbinary disk and the MBHs, rather than to their masses.

2.3. Linking MBH accretion to the host dynamics

In our model, the properties of the accretion flow are connected to the large scale dynamics of the galaxy through the quantity v/σ . However, relevant kinematic and dynamical information about σ is missing in our simple semianalytical model, and we adopt a phenomenological approach to the problem. We postulate that the typical v/σ of the accreting material mirrors that of the stellar and/or gaseous component of the galaxy at much larger scales. The latter has been measured for a variety of galaxy samples, which we use to construct v/σ distributions to implement in our galaxy evolution model. In the following we first describe in details measurements available for the disk and bulge component separately, and then discuss the specific prescriptions employed in our models.

2.3.1. Measurements of v/σ in gaseous disks

Measurements of v/σ for the gas component in spiral galaxies have been obtained with integral field emission line spectroscopy with sub-arcsec resolution, tracing the gas from 10 kpc down to sub-kpc scales, depending on the redshift of the system. More specifically Kassin et al. (2012) discuss explicitly the dependence of v/σ on redshift and stellar mass for disk galaxies at $z < 1.2$ using a sample of several hundred objects. Here, we complement their data with measurement at higher redshift. Wisnioski et al. (2011); Epinat et al. (2012); Swinbank et al. (2012) report v/σ measurement for star forming galaxies in the redshift range $1.2 < z < 1.7$; their data are combined in a catalog of 30 objects that we take as a representative sample at $z \approx 1.5$. Förster Schreiber et al. (2009); Law et al. (2009); Newman et al. (2013) explore the range $1.5 < z < 2.5$; we combine their data in a catalog of 56 objects that we take as a representative sample at $z \approx 2$. Gnerucci et al. (2011) measure v/σ of 33 star forming galaxies at high redshift, in the range $3 < z < 4.8$. They find a fraction of rotating systems (defined as systems having $v/\sigma > 1$) of $\sim 1/3$, claiming that “the comparison between the SINS analysis at $z \sim 2$ and the AMAZE analysis at $z \sim 3.3$ suggests that the fraction of rotating objects does not evolve within this redshift interval”. Unfortunately they do

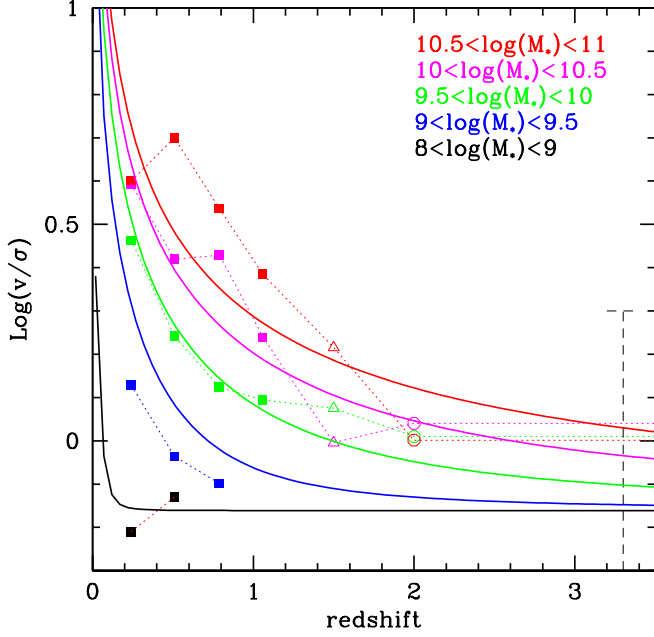


FIG. 4.— v/σ of gas on kpc scales in gas-rich galaxies. Points are derived from the literature: filled squares are derived from Kassin et al. (2012), whereas open triangles and open circles are derived from our $z \approx 1.5$ and $z \approx 2$ samples respectively. Data sets have been grouped and binned as described in the main text. The dashed vertical line at $z = 3.3$ marks the v/σ range reported by Gnerucci et al. (2011). Different colors correspond to different mass bins, as labeled in the figure. Solid lines represent the best fit to the data given by equation (16), evaluated at the middle point of each $\log M_*$ bin. The average dispersion of the measurement of each data point is ≈ 0.34 dex in $\log(v/\sigma)$.

not provide a full set of mass and v/σ measurements for all the objects in their sample. For fitting purposes, we then just assume another set of measurements at $z \sim 3.3$ mirroring the ones at $z \approx 2$. Each data sample is divided into galaxy stellar mass (M_*) bins, and for each mass bin we compute the mean v/σ and the dispersion around the mean. We therefore end-up with a series of measurements of v/σ in the z - M_* plane, that we then fit with a ‘Nuker’s law’ of the form

$$\frac{v}{\sigma} = a \left(\frac{x}{x_0} \right)^\alpha \left[1 + \left(\frac{x}{x_0} \right)^\beta \right]^{-\alpha/\beta}, \quad (16)$$

where $x = \log(1+z)$, and $x_0 = b(\log M_* + c)$. Equation (16) describes a broken power-law where the slope at $x > x_0$ is forced to zero, and the location of the break, x_0 , depends on the stellar mass of the system. The parameter β describes the ‘sharpness’ of the transition between the two power-laws. The best least-square fit to the data gives the following value for the five parameters: $a = 0.6949$; $b = 0.4548$; $c = -8.5255$; $\alpha = -0.8680$; $\beta = 3.2126$. Data and best fit are shown in Figure 4. To account for the data dispersion around the best fit, we assume that the density distribution for v/σ is log-normal with standard deviation of 0.34 dex around equation (16).

2.3.2. Measurements of v/σ in stellar bulges

The kinematics of stellar bulges has been also extensively studied in the literature. The SAURON project (Cappellari et al. 2007) focuses on a sample of 48 ellipticals and lenticular galaxies, completed with 18 objects from the literature, for a total of 66 objects. Kinematic measurements are also available for stellar bulges of spiral galaxies; Fabricius et al.

	light seeds	heavy seeds
M_{cloud}	$3 \times 10^4 M_\odot$	$3 \times 10^4 M_\odot$
$\epsilon_{\text{SN,b}}$	0.4	0.4
$\epsilon_{\text{SN,d}}$	0.1	0.1
f_{jet}	10	10
A_{res}	6×10^{-3}	5.75×10^{-3}
A_{Edd}	2.2	1
k_{accr}	10^{-3}	10^{-3}

TABLE 1
THE CALIBRATED VALUES OF THE FREE PARAMETERS OF THE MODEL (SEE B12 AND SEC. 2.2 FOR THEIR MEANING). THESE VALUES ARE USED TO PRODUCE THE FIGURES.

(2012) report measurements of v/σ for bulges in 43 spiral galaxies of all classes, from S0 to Sc, also making a distinction between bulges and ‘pseudobulges’. Using the total sample of 109 objects, we note that, in general, a distinction can be made between ellipticals and lenticular/spirals. The former have lower v/σ , clustering at zero values, whereas the latter have generally higher v/σ , extending to values greater than 1, and with an average greater than 0.5. Moreover, ‘pseudobulge’ spirals tend to rotate faster than classical bulges, as shown in Figure 5. The v/σ distribution is analytically fitted with the following functions:

- ellipticals

$$f(x) = a e^{b x^c}, \quad (17)$$

with $a = 14.59$, $b = -3.98$, $c = 0.96$;

- all spirals

$$f(x) = a x^b e^{c x^d}, \quad (18)$$

with $a = 42.24$, $b = 1.29$, $c = -2.95$, $d = 2.81$;

- bulges in spirals

$$f(x) = \frac{a}{b} x^b e^{-0.5[(x-c)/b]^2}, \quad (19)$$

with $a = 2.10$, $b = 0.24$, $c = 0.47$;

- pseudobulges in spirals

$$f(x) = \frac{a(x-b)}{x^2 + c x + d}, \quad (20)$$

with $a = 0.083$, $b = -0.53$, $c = -1.38$, $d = 0.50$.

When implemented in our code, we normalize each $f(x)$ so that $\int_0^\infty A f(x) dx = 1$, to get a probability density function (PDF). The v/σ of each individual galaxy is then drawn randomly from the appropriate PDF, according to its morphological type.

2.3.3. Implementation in our galaxy formation model

In our runs we define ellipticals those galaxies with a bulge to total mass ratio $B/T > 0.7$, and spirals the remaining galaxies. Note that in this way we consider spirals also S0 objects, regardless their gas content. However, there are only small differences between the v/σ distributions of these two classes. Since in ellipticals (in particular the most massive ones at lower redshifts) cold gas is subdominant, we always assume that the dynamics of gas feeding the MBH traces that of the stellar population, and we draw v/σ from the PDF

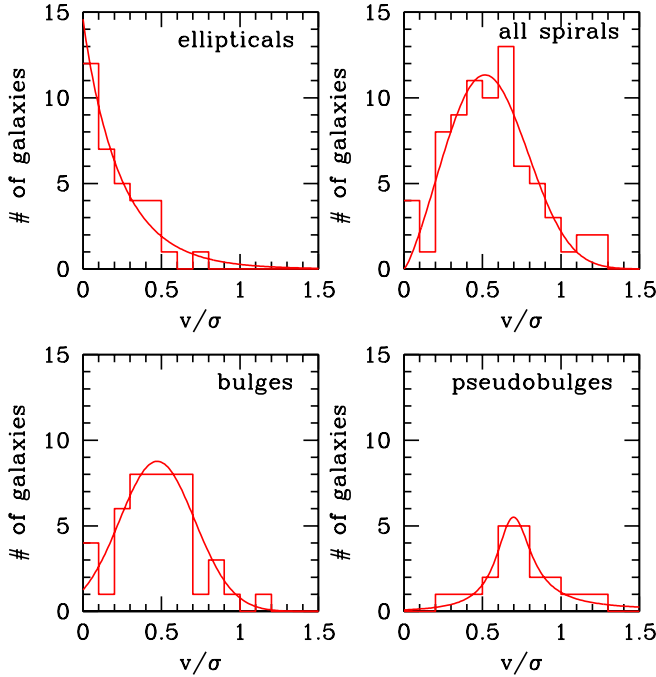


FIG. 5.— Distribution of v/σ for different type of galaxies (as labeled in the panels) at low redshifts. In each panel, the red histogram is the distribution of observed v/σ , and the overlaid curve is the analytical fit reported in the main text.

given by equation (17). Fueling of the MBH in spiral galaxies might be more subtle, being related either to the dynamics of the kpc scale cold gas in the disk or to that of the bulge/pseudobulge. We therefore explore three different models:

- i *disk* model. The dynamics of the MBH fuel has the same kinematic properties of the large scale disk, and v/σ of each spiral is drawn from a log-normal distribution with average given by equation (16) and standard deviation of 0.34 dex;
- ii *bulge* model. The dynamics of the MBH fuel has the same kinematic properties of the bulge; we do not distinguish between bulges and pseudobulges and we extract v/σ from the overall distribution of spiral bulges given by equation (18);
- iii *pseudobulge* model. The dynamics of the MBH fuel has the same kinematic properties of the bulge and we distinguish between bulges and pseudobulges. In our model, spiral bulges form either via disk instabilities or via mergers. In the former case we assume that a pseudobulge forms and we take v/σ from the distribution given in equation (20), in the latter we assume a classical bulge forms and we take v/σ from the distribution given in equation (5).

Every time a given galaxy changes morphology (as a result of mergers, disk instabilities or quiescent evolution) or whenever it undergoes a major merger, it is assigned a new v/σ from the appropriate probability distribution. In the case of minor mergers, instead, we combine the values of v/σ of the merging galaxies, weighing them with their masses. During a quiescent evolution, we keep v/σ fixed in the case of the distributions of equations (17), (18), (5) and (20), and we adiabatically evolve it with redshift and galaxy mass in the

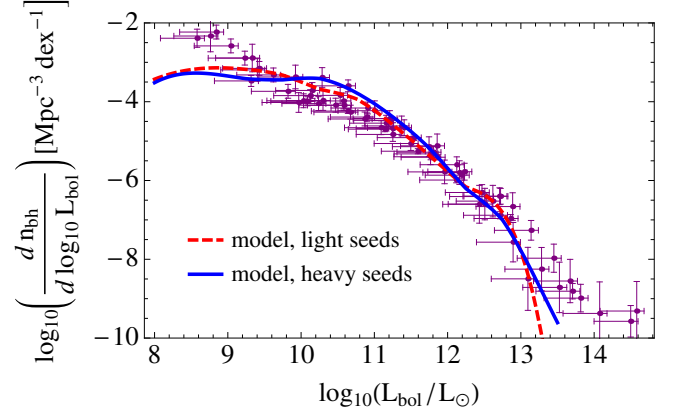


FIG. 6.— The MBH bolometric luminosity function at $z = 0.1$ predicted by our model vs the compilation of observational data by Hopkins et al. (2007). The vertical error bars on the data are from Hopkins et al. (2007), while for the horizontal ones we have assumed -0.5 dex and $+0.1$ dex to account for possible overestimation of the bolometric correction (Lusso et al. 2012).

case of the log-normal PDF with average given by equation (16) (this is because equation (16) does indeed depend on the galaxy mass and redshift).

For the sake of comparison, we also add three models featuring the coherent and chaotic scenarios often used in the literature:

- iv *coherent* model. Each accretion event takes place in a well defined plane, persisting for the duration of the episode and efficiently spinning-up the hole (Thorne 1974); c.f., for instance, the coherent model of Berti & Volonteri (2008);
- v *chaotic I* model. For each accretion event, we always take $F = w = 0.5$, independently of the accreted mass (c.f. for instance the chaotic model of Berti & Volonteri 2008);
- vi *chaotic II* model. The model of this paper, but with $F = 1/2$, i.e., with isotropic distribution for the angular momenta of the gas clouds (King & Pringle 2006).

For each model we performed two sets of runs seeding MBHs either as PopIII remnants at $z \sim 20$ (light seeds) or as endproduct of direct collapse at $z \sim 15$ (heavy seeds); see B12 for more details. Each run consists of ~ 24000 merger trees⁹ in the dark-matter halo mass range $10^{10} - 10^{15} M_\odot$. In this paper we focus on MBHs of $M_{bh} > 10^6 M_\odot$ at relatively low z , our first aim being a comparison with measured spins in the local Universe. Since memory of the seeding process fades away already at high redshift, we did not find any significant difference between the light and heavy seed prescriptions at any considered redshift, for any considered galaxy subsample. We therefore add up light and heavy seed runs to increase the statistics and ‘smoothness’ of our theoretical samples to be compared to the observed data (see section 4.2).

3. RESULTS

3.1. Calibration

As in B12, we anchor our model to a number of observables, with particular attention to quantities characterizing

⁹ For the coherent/chaotic models we make shorter runs with a factor of 20 less halos.

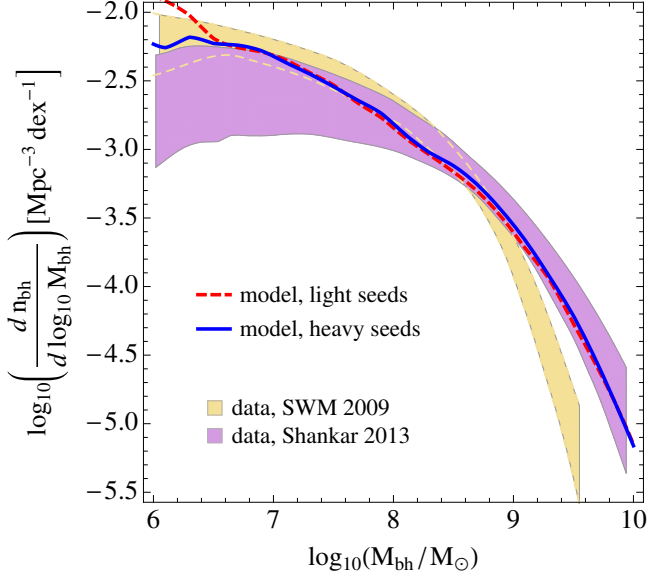


FIG. 7.— The MBH mass function at $z = 0.1$ predicted by our model vs the ranges, reconstructed from observational data, given by Shankar et al. (2009) and Shankar (2013). Note that although the results of Shankar (2013) are still preliminary and are based only on bulge-dominated galaxies, it is clear that systematic errors still dominate the uncertainties in the high-mass end.

the MBH population and their accretion properties in the local $z \sim 0$ universe, where all the currently available MBH spin measurements (which we will use to test our model, c.f. sec. 4) are performed. More precisely, we calibrate the model’s free parameters (c.f. table 1) against observational data for the QSO luminosity function at $z = 0.1$ (Figure 6), the MBH mass function at $z = 0$ (Figure 7), the local “Magorrian” relation between the MBH mass and the bulge dynamical mass in ellipticals (Figure 8), the stellar mass function at $z = 0$ (Figure 10), the observed fraction of galaxies with various morphologies at $z = 0$ (Figure 11), and the star formation density for $0 \leq z \lesssim 5$ (Figure 9). We stress, however, that the results of our model (and the overall conclusions of this paper) do not depend strongly on the values of the free parameters. Also, Figures 6 – 11 are produced with the *pseudobulge* model (c.f. sec. 2.3.3), but the *bulge* and *disk* models produce similar results.

As can be seen (Figure 6), our model produces reasonable results for the $z = 0.1$ QSO luminosity function when compared to the compilation of observational data by Hopkins et al. (2007), despite slightly underestimating it at low luminosities (the disagreement at the high-luminosity end is less statistically significant). The vertical error bars on the data are from Hopkins et al. (2007), while for the horizontal ones we have assumed -0.5 dex and $+0.1$ dex to account for possible overestimation of the bolometric correction (Lusso et al. 2012). Similarly, Figure 7 shows that our predictions for the $z = 0$ black-hole mass function are in agreement with recent estimates by Shankar (2013). While the reconstruction of the MBH mass function performed by Shankar (2013) is still preliminary and based only on bulge-dominated galaxies, from a comparison to the observational estimates of Shankar et al. (2009) (also shown in Figure 7), it is clear that systematic errors still dominate the estimates of the mass function at the high-mass end, and that our model’s prediction is clearly within the observational uncertainties. Figure 8 shows the agreement between a compilation of dynamical bulge masses and black-hole masses in elliptical galaxies from McConnell

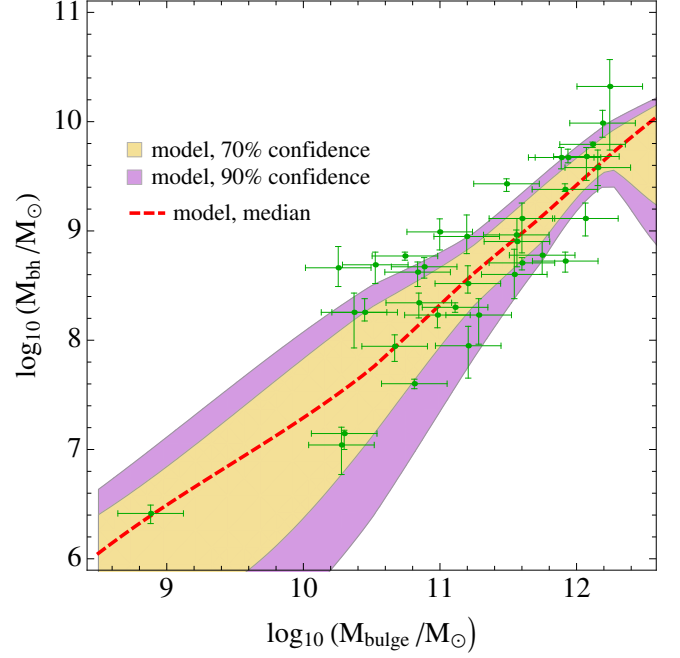


FIG. 8.— The relation between the MBH mass and the dynamical mass of the bulge predicted by our model at $z = 0$, compared to the data compilation of McConnell & Ma (2013). This figure adopts a light-seed model, but the heavy-seed model leads to similar results.

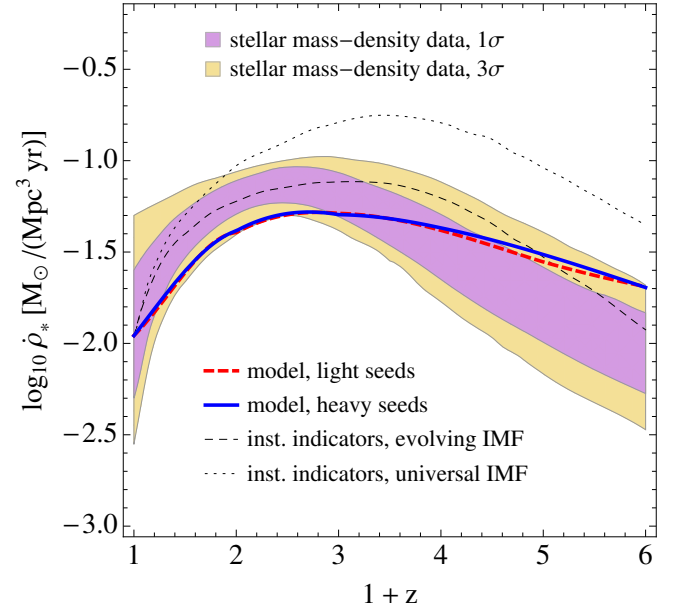


FIG. 9.— The star formation density as function of redshift, as predicted by our model vs the one derived by Wilkins et al. (2008) from observations of the stellar mass density and assuming an evolving IMF (shaded regions, corresponding to 1σ and 3σ confidence regions). We also show fits to instantaneous star-formation density indicators (Wilkins et al. 2008), assuming either a universal or an evolving IMF.

& Ma (2013) (see also Häring & Rix 2004b; Magorrian et al. 1998) and our model’s predictions for ellipticals, which we define as galaxies for which the bulge contributes at least 70% of the total dynamical baryonic mass (see discussion below as well as Guo et al. 2011, B12).

The improved star-formation implementation described in sec. 2.1 allows our model to better reproduce data for the star-formation history than the original prescription of B12. Fig-

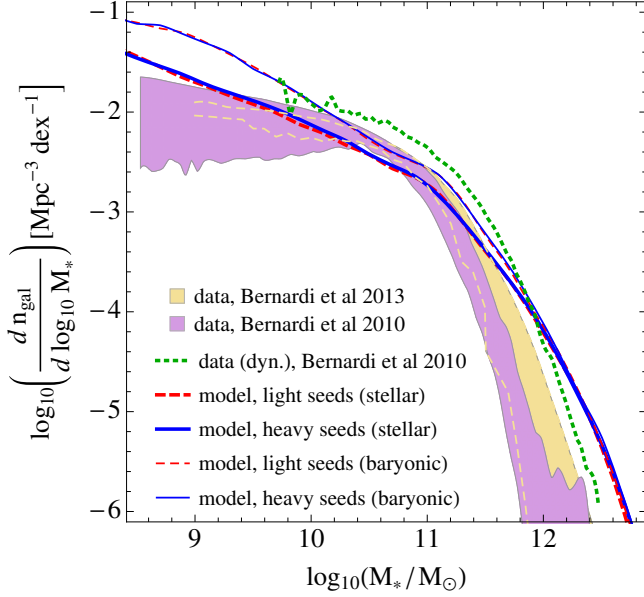


FIG. 10.— The mass function of galaxies at $z = 0$ predicted by our model (including the stellar mass alone, or the total baryonic mass in gas and stars) vs the estimates of Bernardi et al. (2010) and Bernardi et al. (2013) for the stellar-mass function from luminosity observations, and the estimate of Bernardi et al. (2010) for the dynamical mass function (obtained by reconstructing the dynamical masses through the galaxy’s size and velocity dispersion).

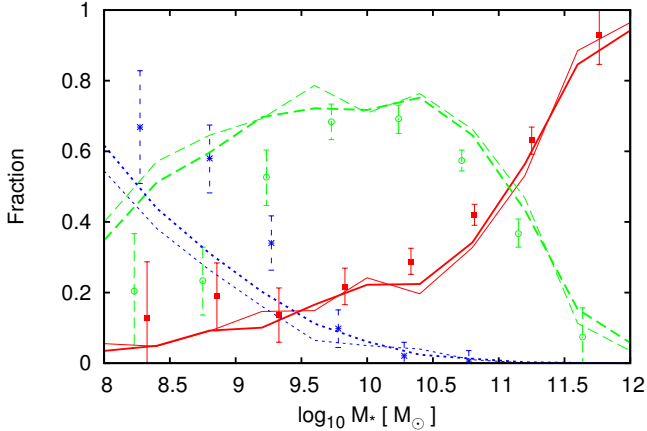


FIG. 11.— Morphologies predicted by our model at $z = 0$ as a function of the stellar mass (thick lines: heavy seeds; thin lines: light seeds), vs data from Conselice (2006) (squares: ellipticals; circles: spirals; stars: irregulars).

ure 9 compares our predictions to reconstructions based either on observations of the stellar mass density and assuming an evolving IMF (Wilkins et al. 2008), or to fits to instantaneous star-formation density observations (Wilkins et al. 2008), assuming either a universal or an evolving IMF. Our predictions for the local galaxy mass function (Figure 10) are instead slightly higher than the observational determinations by Bernardi et al. (2010) and Bernardi et al. (2013) at the low- and high-mass ends. The same problem is often seen in galaxy formation models, which tend to over-produce stars (see, e.g. De Lucia & Blaizot 2007; Guo et al. 2011; Khandai et al. 2014), because of overly-simplified treatments of AGN and supernova feedback. More sophisticated feedback schemes might improve the match with observations, and we plan to investigate this issue further in future work.

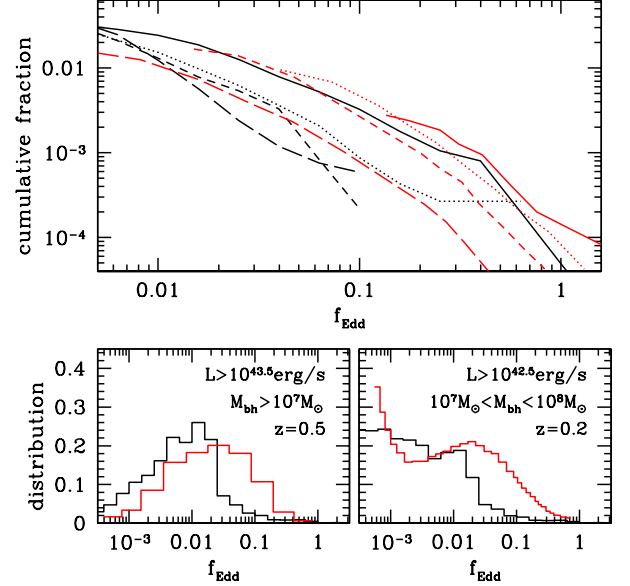


FIG. 12.— Distribution of Eddington ratios f_{Edd} . In the top panel the cumulative fraction of MBHs accreting above a certain Eddington ratio is shown for different MBH mass bins. Black lines show the predictions of our model at $z = 0.1$ for the mass bins $2 \times 10^6 M_\odot < M < 5 \times 10^6 M_\odot$ (solid); $5 \times 10^6 M_\odot < M < 2 \times 10^7 M_\odot$ (dotted); $2 \times 10^7 M_\odot < M < 5 \times 10^7 M_\odot$ (short-dashed); $5 \times 10^7 M_\odot < M < 2 \times 10^8 M_\odot$ (long-dashed). Those are compared with observational estimates from Heckman et al. (2004) (red lines) evaluated at $M_{\text{bh}} = 3 \times 10^6 M_\odot$ (solid); $M_{\text{bh}} = 10^7 M_\odot$ (dotted); $M_{\text{bh}} = 3 \times 10^7 M_\odot$ (short-dashed); $M_{\text{bh}} = 10^8 M_\odot$ (long-dashed). In the bottom panels, the f_{Edd} distribution for selected systems (as labeled in each panel) are compared to data from Hickox et al. (2009) (left) and Kauffmann & Heckman (2009) (right). Black histogram are predictions of our model, red histograms are the data.

However, one should also keep in mind that determinations of the mass function are typically obtained by estimating galaxy masses through their luminosity, which results in large systematic uncertainties (especially at the high-mass end) due to the assumptions on the stellar mass-to-light ratio, as well as the different possible ways in which one can fit the light profiles (Bernardi et al. 2013). Finally, Figure 11 shows the prediction of our model for the fraction of ellipticals, spirals and irregulars as a function of stellar mass, as well as the observational estimates of Conselice (2006). More specifically, in determining our model’s predictions we follow Guo et al. (2011) and B12 and use the fraction of total baryonic mass in the bulge, $f_{\text{morph}} = M_b / (M_b + M_d)$ (with M_b and M_d the bulge and disk masses), to discriminate the various morphologies, i.e. we classify a galaxy as an elliptical when $f_{\text{morph}} > 0.7$, as a spiral when $0.03 < f_{\text{morph}} < 0.7$, and as an irregular when $f_{\text{morph}} < 0.03$.¹⁰ In spite of this simplistic classification, it is clear that our model reproduces, at least qualitatively, the observational results.

Since in section 4 we will be dealing with accreting systems, in Figure 12 we compare the Eddington ratio, f_{Edd} , distribution predicted by our model to observations. In the top panel, we compare the local cumulative distribution of f_{Edd} as measured by Heckman et al. (2004), who inspected 23,000 active galaxies in a complete sample of 123,000 galaxies from the SDSS in the redshift range $0.05 < z < 0.2$, to the predictions of our *pseudobulge* model at $z = 0.1$ (other

¹⁰ Qualitatively similar results are obtained if one uses stellar rather than total baryonic masses to define f_{morph} , but it seems preferable to use total baryonic masses if one wants to apply the same classification to high redshifts, where gas may dominate over stars.

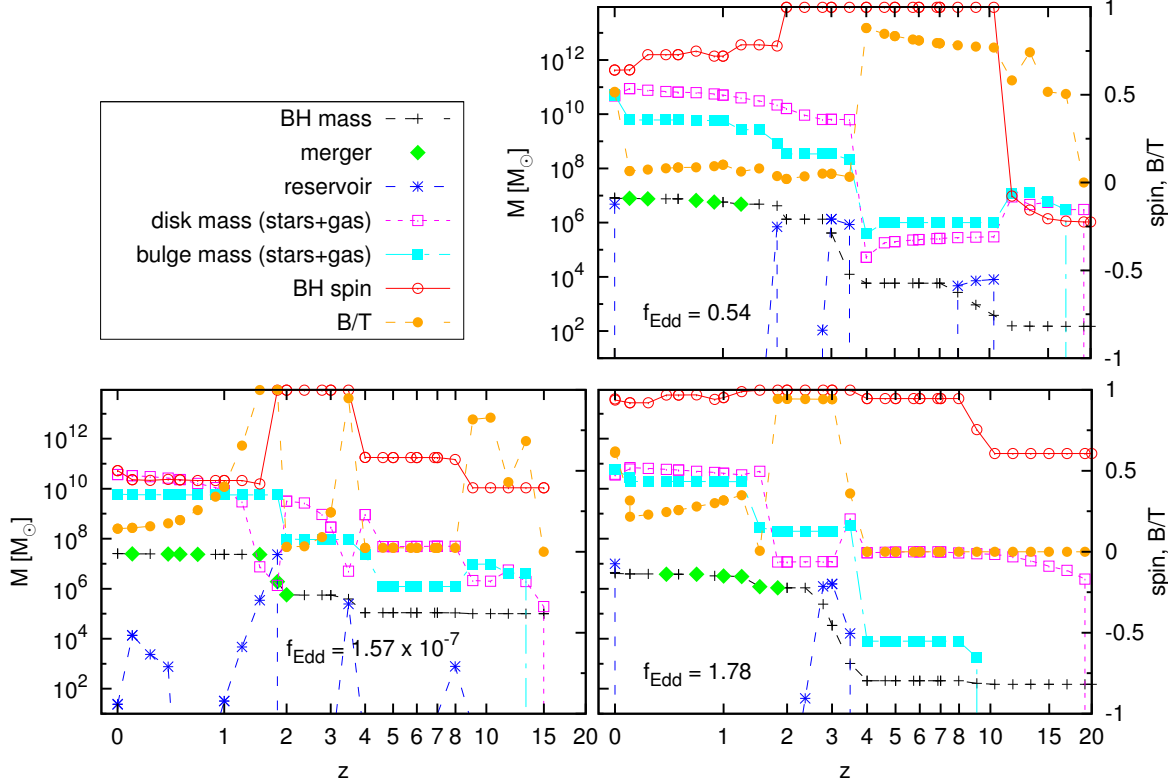


FIG. 13.— Evolutionary tracks of three individual galaxies and MBHs selected among the output of the *bulge* and *pseudobulge* models (we do not distinguish here between the two prescriptions, because they present the very same features). All symbols are explained in the upper left legend.

models yield similar results). The model reproduces the f_{Edd} observed trend satisfactorily, even though we see a paucity of accreting systems at intermediate masses. This is also clear by looking at the lower panels, which highlight the difference between the model and the data at $f_{\text{Edd}} \approx 0.1$. The figure shows that our model catches the main trends in the low redshift Eddington ratio distributions, although not perfectly. A better calibration of the model against this quantity may be considered in future work.

3.2. MBH spin evolution

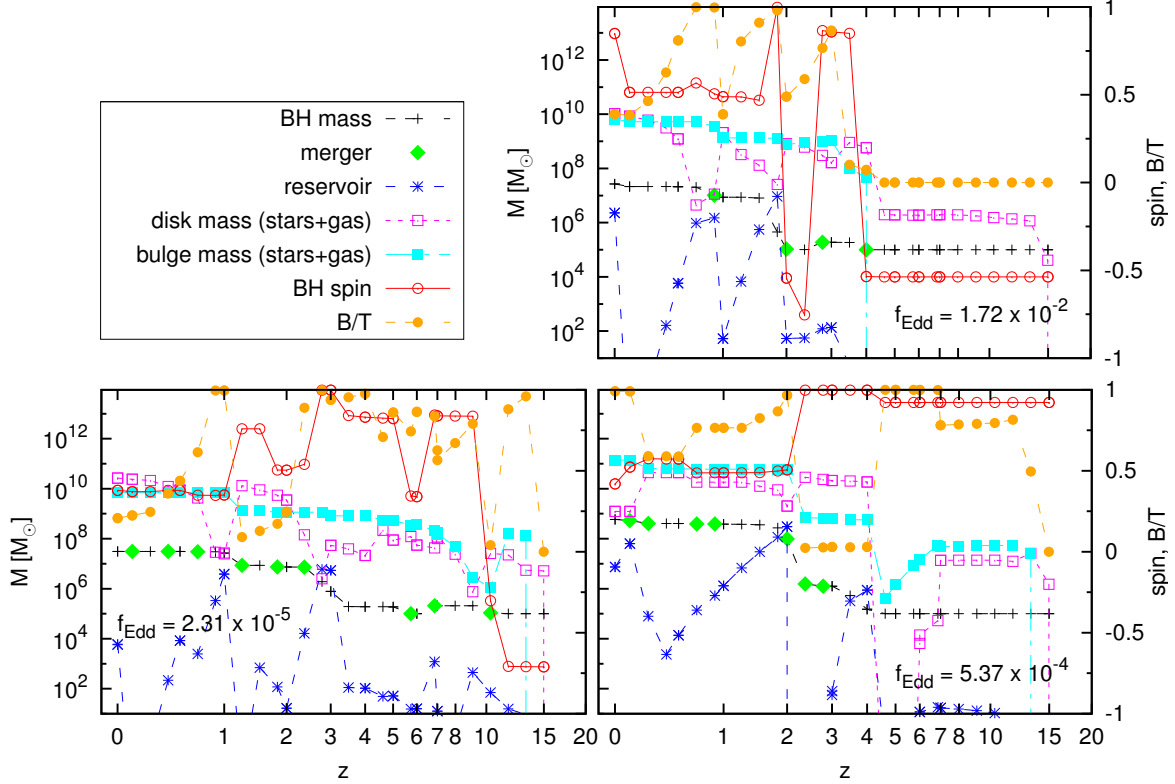
3.2.1. Evolution of individual MBHs

The spin evolution of each MBH is dictated by a complex interplay of *i*) the variable supply of mass available for accretion, *ii*) the time-changing host galaxy morphology following major and minor mergers, disk instabilities, Dark Matter and hot IGM gas accretion, and *iii*) MBH binary coalescence events. We will first inspect some examples of individual MBH-galaxy evolutionary tracks to get a sense of how such interplay impacts the typical values of MBH spins in different types of galaxies. We stress, however, that the cases we consider below have a purely illustrative purpose, and do not represent the whole variety of evolutions predicted by our model. Predictions on statistically significant samples of objects will be presented in section 3.2.2.

Figure 13 gives three examples of evolutions of $z = 0$ spirals for the *bulge* and *pseudobulge* models. The two right panels represent two MBHs accreting at about the Eddington limit at low redshift. Despite the similarity of the two host galaxies, the final spins are quite different. In the bottom panel, the spin grows to almost maximal early on, and

stays above 0.9 most of the time. At $z < 2$, accretion drops and a sequence of minor mergers pushes the spin down a bit; however, the residual low redshift accretion keeps the spin near to its maximal value. In the top panel, a $z \sim 2$ accretion episode dumps the spin to ≈ 0.8 , and the subsequent sequence of minor mergers takes it further down to its final value of ≈ 0.6 . The two different final spins reflect the wide kinematic range of bulges and pseudobulges depicted in Figure 5: a typical v/σ above (below) 1 will result in a maximally (non-maximally) spinning MBHs like the one in the lower (upper) right panel. On the other hand, the very sub-Eddington system shown in the lower left panel has a final MBH spin ≈ 0.5 . In this case, a major merger at $z \approx 2$ changed the morphology of the galaxy from disk to bulge dominated, and the following highly ‘incoherent’ (i.e. with $v/\sigma \ll 1$) accretion caused a dramatic spin down of the MBH. After that episode, the galaxy re-acquired a substantial disk because of minor mergers and accretion episodes, but the accretion rate onto the central MBH did not become high enough to substantially change its spin.

These trends can be compared to those found in the *disk* model, shown in Figure 14. The non-accreting spiral shown in the bottom-left panel is quite similar to its counterpart in the *bulge* model: the MBH acquired a low spin following major mergers and disk instabilities that changed its host’s morphology to bulge dominated; the host galaxy then re-acquired a disk without however triggering sufficient accretion onto the central MBH to change its spin. The situation is quite different for accreting spirals. In the *disk* model, at low redshift, such systems always have $v/\sigma > 1$ (see Figure 4), meaning that any significant accretion episode will bring the MBH to

FIG. 14.— Same as Figure 13, but for the *disk* model.

nearly maximal spin, as shown in the top right panel of Figure 14. Conversely, the bottom right panel shows an example of a MBH hosted in an elliptical. In this case, the distinction between *bulge* and *disk* models becomes less relevant, since in both of them ellipticals share the same dynamics. We see in this case that a sequence of mergers and accretion episodes at $z < 3$ causes a significant spin-down of the central MBH, to ≈ 0.3 .

From the above examples we can draw a couple of conclusions. Non-accreting systems (we arbitrarily put a nominal threshold at $f_{\text{Edd}} = 0.01$) typically retain memory of the last ‘violent’ event that changed the central MBH spin. Since this is likely to be a major merger/disk instability temporarily changing the galaxy morphology to elliptical, the MBH spin will likely be small (non-maximal, in any case), whether the galaxy later retains a bulge-like morphology or acquires a disk again. Highly accreting systems will likely have their spin affected by the ongoing accretion episode. In this case, the final spin depends on the typical v/σ of the host galaxy. Spirals in the *bulge/pseudobulge* models have a range of possible spins mirroring the wide spread in v/σ ; conversely spirals in the *disk* model are almost guaranteed to have maximally spinning MBHs. On the other hand, accreting ellipticals tend to have low spins, because of their typically low v/σ , as shown in Figure 5.

3.2.2. Spin evolution of the global MBH population

Having seen how accretion, mergers and galaxy morphology contribute to the MBH spin make-up, we turn now to the investigation of the cosmic spin evolution of the overall population of MBHs. In the two top panels of Figure 15 we show the spin distributions predicted by the *pseudobulge* (left plot)

and *disk* (right plot) models for selected subsamples of galaxies at different redshifts. Both models feature the same spin evolution prescription for elliptical galaxies, which results in very similar distributions. The overall spin distribution of elliptical galaxies does not evolve much from $z = 5$ to the present day. For $M_{\text{bh}} \lesssim 10^6 M_\odot$, $J_{\text{disk}}/2J_{\text{bh}} > 1$ and MBHs tend to spin fast. At large masses, $J_{\text{disk}}/2J_{\text{bh}} \ll 1$, and a_{bh} tends to the equilibrium value given by Figure (3). In fact, the median v/σ of elliptical galaxies is ≈ 0.2 , corresponding to $F \approx 0.6$, which translates in a median equilibrium spin of 0.3, in good agreement with Figure 15.

The spin evolution of spiral galaxies is instead different in the two models. In the *pseudobulge* model, spiral galaxies show more evolution with redshift with respect to ellipticals, but the general trends are the same for both populations. Note that at large masses, spins are on average larger by virtue of the typically higher v/σ , as shown in Figure 5. In particular, the subset of accreting spirals maintains, on average, higher spins at all redshifts, as discussed in Section 3.2.1. Things are different in the *disk* model: although the overall population of spirals is quite similar to that of the *pseudobulge* model, accreting spirals tend to be maximally spinning, since they generally have $v/\sigma > 1$. The *bulge* model (not shown) yields similar distributions to the *pseudobulge* one.

Distributions for models *coherent*, *chaotic I* and *chaotic II* are shown in the two bottom panels of Figure 15. In the *coherent* model MBHs tend to be maximally spinning irrespectively of redshift, accretion rate and galaxy host morphology. The opposite is true for the *chaotic I* model, where spins tend to be small ($a_{\text{bh}} < 0.5$) and cluster around zero. In the *chaotic II* model, there is a transition between maximally spinning MBHs at low masses and non-spinning MBHs at high masses.

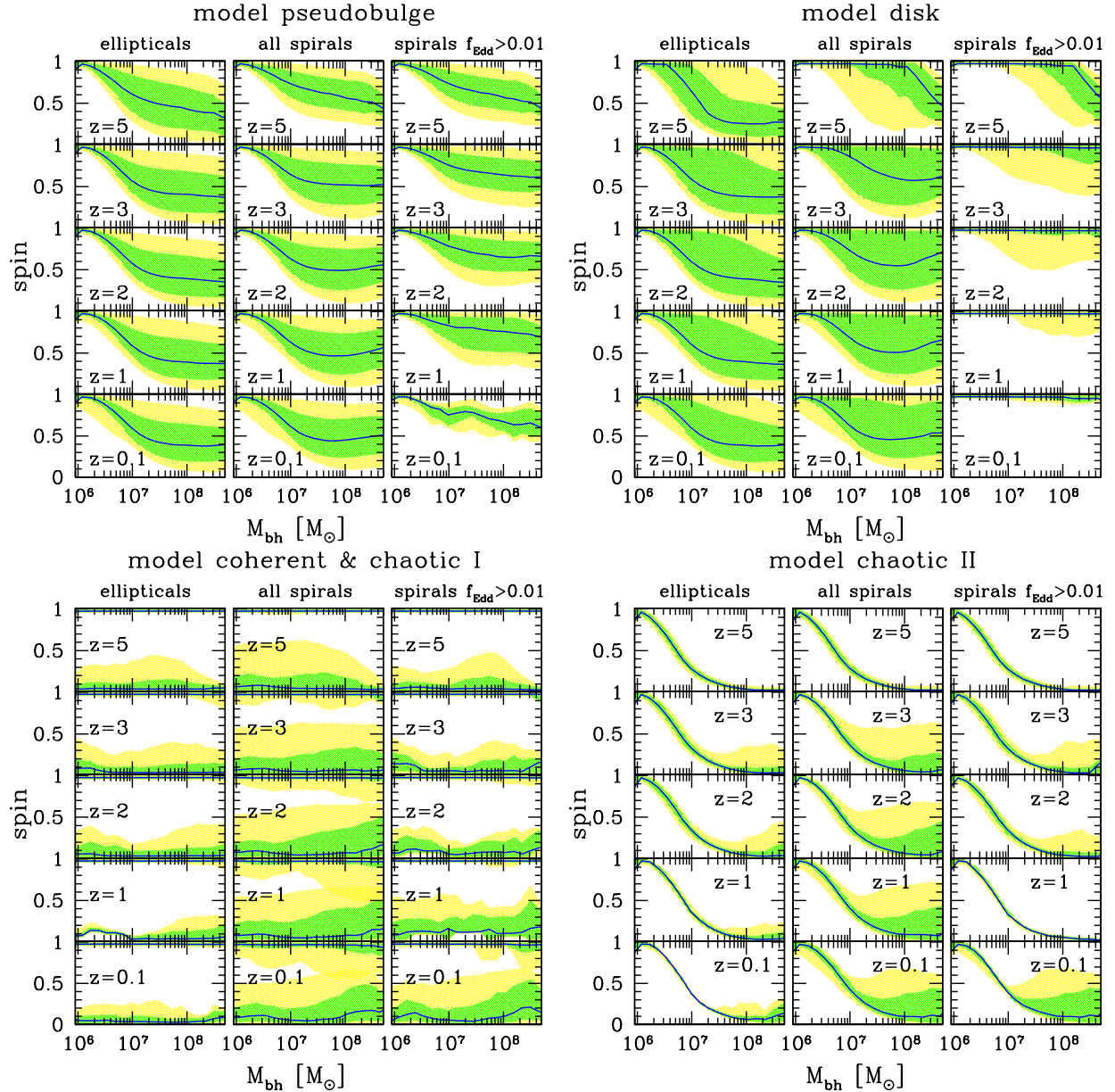


FIG. 15.— Spin evolution as a function of redshift for different subsample of galaxies for the model *pseudobulge* (top-left plot), *disk* (top-right plot), *coherent* and *chaotic I* (bottom-left plot), and *chaotic II* (bottom-right plot). In the bottom-left plot, the *coherent I* model generates the distributions clustered around $a_{\text{bh}} = 1$ and the *chaotic I* model generates the distributions clustered around $a_{\text{bh}} = 0$. In each panel, the blue line is the median of the spin distribution as a function of MBH mass predicted by the model, and green and yellow shaded areas represent the spin ranges where 68% and 95% of the distribution is enclosed.

The difference from the *chaotic I* model is that each cloud of $M_{\text{cloud}} = 3 \times 10^4 M_{\odot}$ has a defined angular momentum (although with random direction); light MBHs align with it and are efficiently spun-up, whereas massive MBHs do not and effectively experience zero-angular momentum accretion averaged over many episodes.

It is interesting to note that as soon as we move away from simplistic accretion prescriptions (i.e., the *coherent*, *chaotic I*, *chaotic II* scenarios), the predicted spin distributions are generally different for different classes of galaxies, which is a testable prediction. In general, MBHs in ellipticals tend to spin lower than their spiral counterparts, but still with an average value of $a_{\text{bh}} \approx 0.4$ and a long tail extending to much higher values. Therefore, our findings do not rule out spin-powered jet models. Indeed, in such models the power of the

jet is usually $\propto a^2$ (Blandford & Znajek 1977; Tchekhovskoy et al. 2010; Narayan et al. 2013), implying a difference of just a few in luminosity between maximally and mildly spinning MBHs. Moreover, accreting MBHs tend to be biased toward higher spins, especially if located in spiral galaxies. In the following, we will compare our model predictions with spin measurements available today at $z < 0.1$. In the future, space-based gravitational wave detectors such as eLISA (Consortium et al. 2013) will allow precise spin measurements of merging MBH binaries up to high redshift, making a comprehensive study of the MBH spin distribution throughout cosmic history possible.

4. COMPARISON WITH OBSERVATIONS

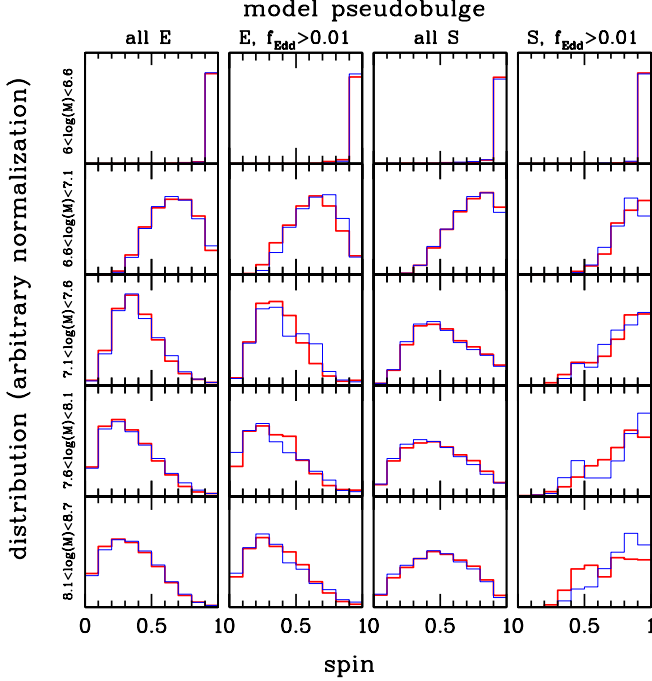


FIG. 16.— Spin distributions predicted by model *pseudobulge* for different galaxy subsample and in different mass bins (as labeled in the figure). Thick-red histograms are computed at $z = 1$, thin-blue histograms at $z = 0.5$.

We carry out here, for the first time, a quantitative comparison between empirical MBH spin measurements and the output of theoretical models self-consistently linking the MBH spin evolution to the properties of the galaxy host. Spin measurements are, however, sparse and bring with them several statistical and systematic uncertainties which are often difficult to quantify. The results of the following analysis should therefore be taken as indicative. Nonetheless, we will show that even with the current data, we can rule out some mass and spin growth scenarios, and gain some qualitative insights about the connection between spin evolution and the properties of the galaxy host supplying gas to the accretion flow.

4.1. The observed sample

MBH spins have been measured via modeling of the $K\alpha$ reflection broad line for about 20 objects. We took data from the sample compiled by Reynolds (2013), integrated with objects from Brenneman (2013). We noted some (minor) discrepancies in the numbers reported by the two Authors; when necessary we inspected the original measurement papers (see references in Reynolds (2013) and Brenneman (2013)) and obtained the values directly from there. All the relevant properties of the sample are shown in table 2. A meaningful comparison to a theoretical model is possible only if *i*) observations have meaningful errors and *ii*) the general properties of the observed subsample can be isolated and selection effects are understood. Both issues are somewhat tricky here.

Errors quoted in table 2 represent 68% confidence level in the mass and 90% confidence level in the spin measurements. A complete knowledge of the probability density functions (PDF) of those quantities would be desirable, but such information is often missing in the literature, and we can at best put forward educated guesses. As for the MBH mass, we consider *i*) a Gaussian PDF with σ equal to the quoted error when the latter is symmetric with respect to the best measured value, *ii*) a flat PDF within the given errors when those are asymmet-

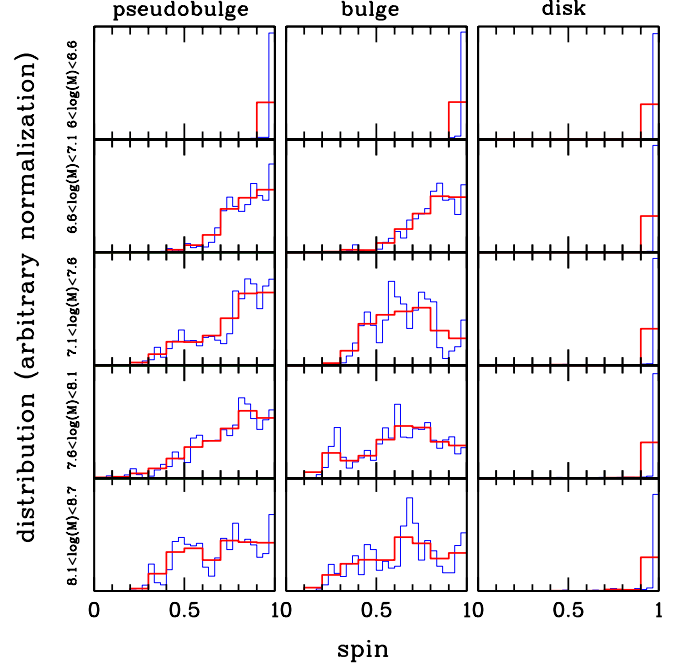


FIG. 17.— Spin distributions for accreting spirals predicted by our models in different mass bins (as labeled in figure) at $z = 1$. Thick-red and thin-blue histograms are computed using 10 and 30 a_{bh} bins respectively.

ric and *iii*) a Gaussian PDF with an arbitrary $\sigma = 0.3$ when errors are absent. Spin PDFs are instead derived by visually inspecting the function $\chi^2(a_{\text{bh}})$, which is always given in the relevant papers. We identify three families of measurements: *i*) sometimes $\chi^2(a_{\text{bh}})$ has an approximately flat minimum, and in this case we take a flat PDF in the corresponding range; *ii*) for few objects $\chi^2(a_{\text{bh}})$ is extremely skewed on the left of the minimum, and in such cases we take as PDF the left half of a Gaussian distribution; *iii*) more often, $\chi^2(a_{\text{bh}})$ is quite symmetric (at least in the 99% confidence region), calling for a Gaussian model of the PDF. Details of the PDFs are given in the last column of table 2. Being aware of the arbitrary nature of this procedure, we also considered an alternative model in which we took all errors in masses and spins to have a flat PDF within the range quoted in column 7 of table 2. We will see in the following that our results are largely independent of the adopted shape of the PDFs.

The obvious selection effect for a $K\alpha$ line measurement, is that the source has to be bright in hard X; in fact most of the MBHs in the sample resides in Seyfert 1 or narrow line Seyfert 1 (NLS1) galaxies. Hosts are usually spirals or lenticular galaxies, with the exception of Mrk841. The observed sample is neither flux nor volume limited. X-ray luminosities and associated MBH masses have distributions consistent with being log-flat in the ranges $10^{42} - 10^{45} \text{ erg s}^{-1}$ and $10^6 - 3 \times 10^8 M_{\odot}$ respectively. Eddington ratios f_{Edd} are also evenly distributed in the range 0.01-1. The redshift distribution is also approximately flat in the range $0 < z < 0.07$, with two outliers at $z > 0.1$. Given these facts, the best matching sample in our model is provided by spiral galaxies (defined by $B/T < 0.7$) with $f_{\text{Edd}} > 0.01$ at low redshift. For the purpose of the analysis, we will therefore exclude Mrk841 (which is an elliptical) and include all galaxies in the observed sample with unknown morphology (thus implicitly assuming they are spirals/lenticulars). Discarding the latter would weaken (because there would be 12 objects only in the observed sample) but not qualitatively change our results.

Object name	Galaxy type	z	$L_X [\text{erg s}^{-1}]$	f_{Edd}	$\log(M_{\text{bh}} [M_\odot])$	spin	adopted PDF
1H0707-495	—	0.0411	3.7×10^{43}	1.0	6.70 ± 0.4	> 0.97	flat [0.97,0.998]
Mrk1018	S0	0.043	9.0×10^{43}	0.01	8.15	$0.58^{+0.36}_{-0.74}$	flat [0,0.94]
NGC4051	SAB(rs)bc	0.0023	3.0×10^{42}	0.03	6.28	> 0.99	flat [0.99,0.998]
NGC3783	SB(r)ab	0.0097	1.8×10^{44}	0.06	7.47 ± 0.08	> 0.88	flat [0.88,0.998]
1H0419-577	—	0.104	1.8×10^{44}	0.04	8.18 ± 0.05	> 0.89	flat [0.85,0.998]
3C120	S0	0.033	2.0×10^{44}	0.31	$7.74^{+0.20}_{-0.22}$	> 0.95	flat [0.95,0.998]
MCG-6-30-15	E/S0	0.008	1.0×10^{43}	0.4	6.65 ± 0.17	> 0.98	hGauss [0.998,0.01]
Ark564	SB	0.0247	1.4×10^{44}	0.11	< 6.90	$0.96^{+0.01}_{-0.06}$	hGauss [0.96,0.04]
TonS180	—	0.062	3.0×10^{44}	2.15	$7.30^{+0.60}_{-0.40}$	$0.91^{+0.02}_{-0.09}$	hGauss [0.94,0.067]
RBS1124	—	0.208	1.0×10^{45}	0.15	8.26	> 0.97	hGauss [0.998,0.02]
Mrk110	—	0.0355	1.8×10^{44}	0.16	7.40 ± 0.09	> 0.89	Gauss [0.945,0.033]
Mrk841	E	0.0365	8.0×10^{43}	0.44	7.90	> 0.52	Gauss [0.80,0.17]
Fairall9	Sc	0.047	3.0×10^{44}	0.05	8.41 ± 0.11	$0.52^{+0.19}_{-0.15}$	Gauss [0.6,0.1]
SWIFTJ2127.4+5654	SB0/a(s)	0.0147	1.2×10^{43}	0.18	7.18 ± 0.07	0.6 ± 0.2	Gauss [0.6,0.1]
Mrk79	SBb	0.0022	4.7×10^{43}	0.05	7.72 ± 0.14	0.7 ± 0.1	Gauss [0.7,0.1]
Mrk335	S0a	0.026	5.0×10^{43}	0.25	7.15 ± 0.13	$0.83^{+0.09}_{-0.13}$	Gauss [0.81,0.067, < 0.92]
Ark120	Sb/pec	0.0327	3.0×10^{45}	1.27	8.18 ± 0.12	$0.64^{+0.19}_{-0.11}$	Gauss [0.68,0.093]
Mrk359	pec	0.0174	6.0×10^{42}	0.25	6.04	$0.66^{+0.30}_{-0.54}$	Gauss [0.66,0.33, < 0.96]
IRAS13224-3809	—	0.0667	7.0×10^{43}	0.71	7.00	> 0.987	Gauss [0.989,0.002]
NGC1365	SB(s)b	0.0054	2.7×10^{42}	0.06	$6.60^{+1.40}_{-0.30}$	$0.97^{+0.01}_{-0.04}$	Gauss [0.97,0.03, < 0.98]

TABLE 2

SAMPLE OF MBHS WITH SPIN MEASUREMENTS FROM $K\alpha$ REFLECTION LINE. THE TABLE IS COMPILED USING OBJECTS FROM REYNOLDS (2013); BRENNEMAN (2013); GALAXY REDSHIFTS ARE TAKEN FROM THE NED DATABASE ^a. QUOTED ERRORS IN THE MASS AND SPIN MEASUREMENTS CORRESPOND TO 68% AND 90% CONFIDENCE LEVEL RESPECTIVELY. THE SPIN PDF WE USE IN OUR STATISTICAL ANALYSIS IS GIVEN IN THE LAST COLUMN, WHICH IDENTIFIES THREE DIFFERENT FUNCTIONAL FORMS: FLAT (MIN AND MAX VALUE GIVEN IN []), HALF GAUSSIAN (MAXIMUM AND σ GIVEN IN []), AND GAUSSIAN (MAXIMUM AND σ GIVEN IN []). IN THE LATTER CASE, A THIRD NUMBER IN [], WHEN PRESENT, DEFINES A SHARP CUTOFF IN THE PDF.

^a<http://ned.ipac.caltech.edu/>

4.2. The theoretical sample

Theoretical distributions are computed on a grid in the $M_{\text{bh}} - a_{\text{bh}}$ parameter space. The MBH mass range $10^6 M_\odot < M_{\text{bh}} < 5 \times 10^8 M_\odot$ is divided in five equally log-spaced bins, and for each bin, spin distributions are computed on ten linear bins covering the range $0 < a_{\text{bh}} < 1$. We applied Gaussian Kernel smoothing to each measured spin, with $\sigma = 0.05$, to get smoother distributions ¹¹. To check the robustness of our results against spin binning, we also constructed two theoretical distributions using 20 and 30 linear a_{bh} bins, and one distribution considering 20 bins both in mass and spin. Results will be given for all the binning choices.

As mentioned above, all but one MBH with spin measurements are accreting at $f_{\text{Edd}} > 0.01$ and reside in spiral or lenticular galaxies at $z < 0.1$. In our runs, although present in a fair number, those systems are rare enough that it is difficult to construct a smooth 2D mass-spin distribution to compare to observations, even by adding together light and heavy seed runs. Figure 15, however, shows that the overall spin evolution of the galaxy population is small at $z < 1$, as a consequence of the reduced galactic activity both in terms of gas cooling/star formation and mergers. This is also shown in Figure 16; here we take model *pseudobulge* and we consider the subsamples of ellipticals (E) vs Spirals/Lenticular (S), also isolating the subsamples of systems accreting with $f_{\text{Edd}} > 0.01$. A visual inspection indeed reveals that there is little difference between any considered spin distribution at $z = 1$ and at $z = 0.5$. Pushing this comparison to $z = 0.1$ we find similar results, even though the distributions are significantly noisier. Based on this evidence, we will therefore

compare observations to theoretical distributions at $z = 1$. We stress, however, that a comparison between the measured spins and the statistical poorer samples obtained from our runs at $z = 0.5$ and $z = 0.1$ yields qualitatively and quantitatively analog results to the $z = 1$ case. The spin distributions adopted in our analysis are shown in Figure 17 for the *pseudobulge*, *bulge* and *disk* models in all mass bins, assuming 10 and 30 a_{bh} bins. In the latter case, distributions are noisier and suffer of small number statistics issues. We will return on this point later in our analysis.

The predicted spin distributions of accreting spirals at low redshift are shown in Figure 18, together with measurements tabulated in table 2. Both the *pseudobulge* and the *bulge* (not shown) models yield similar results, and qualitatively reproduce the observed trends, with most of the measurements and relative errorbars falling in the 95% confidence region predicted by the models. On the contrary, the *disk* (*coherent*) model displays a poorer match with observations: 6 (8) best spin estimates fall outside the predicted 95% confidence region, and there is only a hint in the models of the general spindown observed with increasing MBH mass. Both *chaotic I* and *chaotic II* models result in a very different distribution favoring low spins, which is impossible to reconcile with observations.

4.3. 2D-Kolmogorov-Smirnov test

Although the qualitative comparison between theoretical models and measurements is encouraging (in the sense that we find the right trends in the right subset of galaxies to be compared to observations), and seems to favor the *pseudobulge-bulge* models over the others, we want to corroborate our findings with some more quantitative indicators. We first performed two dimensional, one sample Kolmogorov-Smirnov tests (2D-KS, Press et al. 1992) to compare the ob-

¹¹ The Gaussian Kernel smoothing has mostly the effect of making the distribution visually smoother, and we checked that the results of our analysis are independent of it.

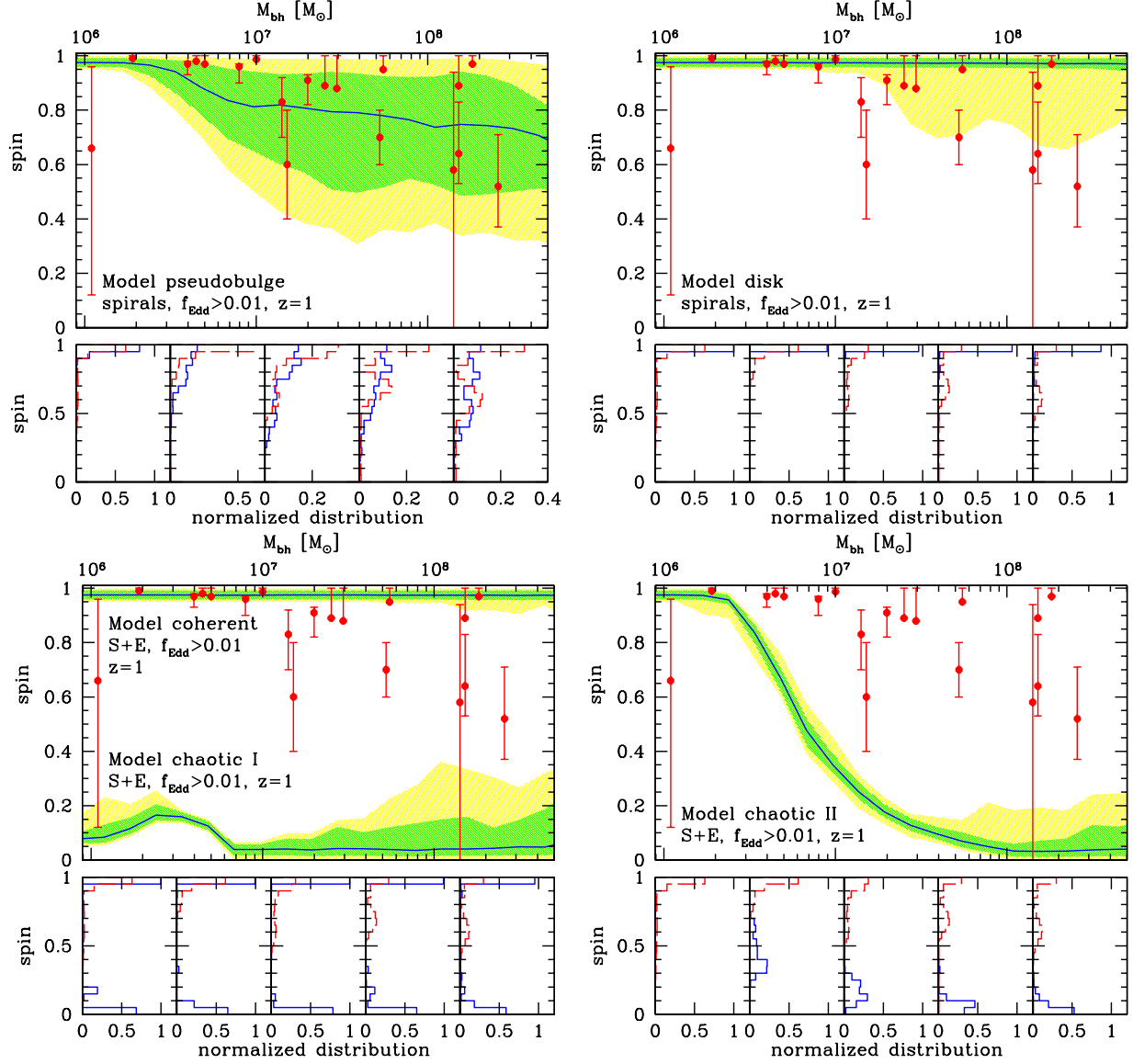


FIG. 18.— Comparison between measured MBH spins and predictions of our models for the subsample of accreting spirals. In all four plots, the top panel shows the outcome of the model with the same line and color-code as in Figure 15 and red dots are measurements with errors as described in table 2. The five small bottom panel show the spin distributions predicted by our models in different mass bins (as labeled in Figure 16, blue solid histogram) and the PDF of the measured spins in the same mass bin, including observation errors (red dashed histograms). The bottom-left panel shows both models *coherent* and *chaotic I*. Theoretical distributions are taken at $z = 1$.

assumptions	pseudobulge			disk			coherent	chaotic I	chaotic II
	E	S	S acc	E	S	S acc	S+E acc	S+E acc	S+E acc
$z = 1 / 10a_{bh} / \text{Gauss}$	0.0015	0.0247	0.2468	0.0017	0.1237	0.1032	0.0719	1.2×10^{-7}	1.4×10^{-5}
$z = 1 / 20a_{bh} / \text{Gauss}$	0.0020	0.0271	0.3614	0.0017	0.1440	0.0081	0.0035	8.7×10^{-8}	2.7×10^{-5}
$z = 1 / 30a_{bh} / \text{Gauss}$	0.0015	0.0302	0.3785	0.0017	0.1453	0.0018	0.0007	1.1×10^{-7}	1.1×10^{-5}
$z = 0.5 / 10a_{bh} / \text{Gauss}$	0.0019	0.0197	0.2666	0.0021	0.0836	0.0835	0.0869	3.5×10^{-7}	1.3×10^{-5}
$z = 1 / 10a_{bh} / \text{flat}$	0.0034	0.0280	0.2336	0.0037	0.1565	0.1030	0.0685	8.3×10^{-8}	2.6×10^{-5}

TABLE 3

2D-KS TEST RESULTS ON DIFFERENT SAMPLES OF GALAXIES FOR ALL SPIN EVOLUTION MODELS UNDER DIFFERENT ASSUMPTIONS ABOUT THE THEORETICAL DISTRIBUTION'S COMPUTATION AND THE TREATMENT OF OBSERVATIONAL ERRORS (INDICATED IN COLUMN 1). FOR THE MODELS *pseudobulge* AND *disk* WE TEST ELLIPTICALS (E) SPIRAL (S) AND ACCRETING SPIRALS (S ACC), WHEREAS FOR MODELS *coherent*, *chaotic I* AND *chaotic II* WE ADD ALL ACCRETING GALAXIES (S+E ACC) UP TO GET BETTER STATISTICS.

served samples to the different MBH subsamples at $z = 1$. Although not as rigorous as its one dimensional counterpart, the test returns an approximate probability, p_{KS} , that the data are drawn from the model distribution (see, Press et al. 1992, for details about the 2D-KS statistics).

To account for observational errors, we computed the average p_{KS} over 10^4 realizations of the observed samples, picking the mass and spin of each individual object from the corresponding PDF. Looking at the results shown in table 3, a number of conclusions can be drawn:

- the selected subsample matters. In particular ellipticals and non-accreting spirals (E and S) have a spin distribution that poorly matches observations yielding $p_{KS} \approx 10^{-3}$ and $p_{KS} \approx 10^{-2}$ respectively for the *pseudobulge* model;
- in the *pseudobulge* model, the subsample of accreting spirals (S acc) is consistent with the observed sample (the *bulge* model, not shown, yields similar results but with slightly smaller p_{KS});
- the *pseudobulge* model is favored, yielding $p_{KS} > 0.20$ independently of binning, redshift and observational error PDF;
- in the *disk* model, accreting spirals provide a reasonable match with observations, but this result is heavily binning dependent;
- the *coherent*¹² model shows features similar to the *disk* model. The agreement with observations is slightly worse and is again binning dependent;
- the two *chaotic* models are ruled out at high confidence, yielding $p_{KS} \approx 10^{-7}$ (*chaotic I*) and $p_{KS} \approx 10^{-5}$ (*chaotic II*).

Although apparently problematic, the bin-dependency of the results for the *disk* and *coherent* models has a physical origin. In our thin accretion disk model, the maximum MBH spin is $a_{bh} = 0.998$ (Thorne 1974). Basically all the MBHs falling in the highest a_{bh} bin have indeed this spin value. By binning the spin distribution, we are ‘spreading’ those systems in the width of the bin; the larger the bin, the larger the spread, making it easier to reconcile the theoretical distribution with the large number of spins measured in the [0.85,1] range (c.f. table 2). If the maximum MBH spin is indeed $a_{bh} = 0.998$ then the finest spin binning should provide the most trustworthy results. We caution, however, that such a narrow spin distribution, peaked close to the maximal spin, is affected by some simplifications that we make in our spin evolution model. As described in Section 2.2, we assume *i*) that at the beginning of each accretion episode the MBH spin is parallel to the global angular momentum of the system, and *ii*) that whenever $J_{disk}/2J_{bh} > 1$ accretion spins the MBH up. Relaxing these two assumptions would affect the highly spinning MBHs, because when $a_{bh} \approx 1$, a small amount of retrograde accretion can efficiently spin the black hole down. The effect of relaxing assumption *i*) has already been discussed in Section 2.2, so here we will simply estimate the effect of relaxing prescription *ii*). For a broad range

¹² In the analysis of the *coherent* and *chaotic* models, we summed-up ellipticals and spiral galaxies to get better statistics. Since in those scenarios the accretion prescription does not depend on the morphology, the two samples share the same spin distribution.

of MBH masses, $J_{disk}/2J_{bh}$ can be larger but still close to 1. In these cases, if the accretion event is initially misaligned with respect to J_{bh} by more than $\pi/2$, accretion would be retrograde during the first part of the spin realignment process. If a fraction of 10% of the gas mass were accreted on retrograde orbits, the equilibrium spin would be the same as in the case $F \approx 0.9$ when neglecting the spin re-alignment, i.e. $a_{eq} \approx 0.9$ (see Figure 3). Such an effect has been observed and discussed in studies where the spin direction was evolved during each single accretion event (Dotti et al. 2010, 2013). Furthermore, different accretion disk models can spin the MBH up only to $a_{bh} = 0.9-0.95$ only (e.g. Gammie et al. 2004); it is therefore impossible to rule completely out the *disk* and *coherent* models. Conversely, we note that the *bulge* and *pseudobulge* models do not suffer from a similar issue because their predictions do not cluster around the maximal spin $a_{bh} \approx 1$ for $M_{bh} > 10^7 M_\odot$, thus yielding consistent results independently of binning.

4.4. Bayesian model selection

Following Sesana et al. (2011), assuming that the observations are uncorrelated, the number of objects, n_i , measured in a particular $\Delta M_{bh} \Delta a_{bh}$ bin, \mathcal{B}_i , in parameter space will be drawn from a Poisson probability distribution with parameter r_i equal to the rate integrated over the bin:

$$p(n_i) = \frac{(r_i)^{n_i} e^{-r_i}}{n_i!}. \quad (21)$$

If we divide the parameter space up into a certain number K of bins, then the information that comes from the *data* (D) is the number of events in each bin. The overall *likelihood* $p(D|X)$ of seeing this data under the model X is the product of the Poisson probabilities for each bin

$$p(D|X) = \prod_{i=1}^K \frac{(r_i(X))^{n_i} e^{-r_i(X)}}{n_i!}. \quad (22)$$

It is straightforward to take the limit of this expression as the bin sizes tend to zero to derive a continuum version of this equation (Gair et al. 2010), but in this analysis we will stick to binned distributions. In the presence of measurement errors, the j -th event can then be assigned to different bins, with a probability given by its PDF $\rho_j(M_{bh}, a_{bh})$. We can therefore construct the entire set of possible array of events falling in each bin, n_i , with their relative probabilities. Each array is then analyzed and weighted according to its probability to get the overall likelihood of the sample given the model.

If we want to compare two competitive models A and B , Bayes’ theorem allows us to assign to model A a probability

$$p(A|D) = \frac{p(D|A)P(A)}{p(D|A)P(A) + p(D|B)P(B)}, \quad (23)$$

whereas probability of model B is just obtained by swapping A and B in equation (23). Here, $p(D|X)$ is the likelihood given by equation (22) and $P(X)$ is the prior probability assigned to model X . The odds ratio of model A over model B is

$$\Lambda_{AB} = \frac{p(D|A)P(A)}{p(D|B)P(B)}. \quad (24)$$

If we do not have any reason to prefer a priori model A to model B , then $P(A) = P(B) = 0.5$, and the odds ratio becomes the likelihood ratio. Moreover, equation (23) implies

assumptions	pseudobulge/disk		
	$\log \Lambda_{pd}$	$p_{\text{pseudobulge}}$	p_{disk}
$z = 1 / 10a_{bh} / \text{Gauss}$	2.936	>0.998	1.2×10^{-3}
$z = 1 / 20a_{bh} / \text{Gauss}$	4.923	>0.999	1.2×10^{-5}
$z = 1 / 30a_{bh} / \text{Gauss}$	8.006	>0.999	9.9×10^{-9}

TABLE 4

MODEL SELECTION RESULTS: COMPARISONS BETWEEN MODELS *pseudobulge* AND *disk*. WE REPORT THE LOG OF THE LIKELIHOOD RATIO, THE PROBABILITY OF MODEL *A* AND THE PROBABILITY OF MODEL *B*.

assumptions	$\alpha \text{ max } \log L$	$\alpha \text{ max } p_{KS}$
$z = 1 / 10a_{bh} / \text{Gauss}$	0.58	0.55
$z = 1 / 10a_{bh} / \text{flat}$	0.58	0.53
$z = 0.5 / 10a_{bh} / \text{Gauss}$	0.56	0.59
$z = 1 / 20a_{bh} / \text{Gauss}$	0.74	0.74
$z = 0.5 / 20a_{bh} / \text{Gauss}$	0.71	0.74
$z = 1 / 30a_{bh} / \text{Gauss}$	0.75	0.81
$z = 0.5 / 30a_{bh} / \text{Gauss}$	0.77	0.81

TABLE 5

MIXING α PARAMETER FOR THE MODEL $\alpha[\text{pseudobulge}] + (1 - \alpha)[\text{disk}]$ THAT MAXIMIZES THE LOG LIKELIHOOD OF THE DATA GIVEN THE MODEL (COLUMN 2), AND THE KS PROBABILITY (COLUMN 3). THE MIXED MODEL HAS BEEN CHECKED AT DIFFERENT REDSHIFTS AND UNDER DIFFERENT ASSUMPTIONS OF SPIN BINNING AND OBSERVATIONAL ERROR PDF, AS INDICATED IN COLUMN 1.

that, in a two model comparison, we can simply assign a ‘relative probability’ $p_A = p(D|A)/(p(D|A) + p(D|B))$ to model *A*, and $p_B = 1 - p_A$ to model *B*.

4.4.1. Odds ratios

We compute odds ratios of models *pseudobulge* (*p*), *bulge* (*b*) and *disk* (*d*) according to equation (24), where we assume $P(A) = P(B) = 0.5$. We consider the sample of accreting spirals at $z = 1$ and different a_{bh} binnings. Likelihoods are computed according to equation (22), folding-in measurement errors. The shape of the error PDFs of each single observation are described in section 4.1, and we factorize $\rho_j(M_{bh}, a_{bh}) = g(M_{bh})h(a_{bh})$, assuming uncorrelated mass and spin measurements.

Results are shown in table 4. As demonstrated by the 2D-KS tests, the consistency of the *disk* model with observations is highly dependent on the binning size of the distribution. This is confirmed by our model selection exercise. If we consider 10 a_{bh} bins, $\log \Lambda_{pd}$ is only ≈ 2.9 , and the *pseudobulge* model provides a better description of the data at a 99.9% confidence level. This is particularly interesting, because even though the *disk* model computed on 10 a_{bh} bins does not fail the 2D-KS test, the odds ratio test provides compelling evidence in favor of the *pseudobulge* model. If we increase the number of a_{bh} bins to 30, we get $\log \Lambda_{pd} \approx 8$, and the *disk* model can be safely ruled out. In contrast, no such trend is seen in the *pseudobulge* vs *bulge* selection (not reported in the table). For any bin size, we find that $\log \Lambda_{pb}$ stays in the range $1 - 1.2$ implying a preference for the *pseudobulge* model, but not at a high statistical significant level. To corroborate these results we also computed odds ratios at $z = 0.5$ and $z = 0.1$ finding analog results (although the statistics is poorer). The comparison *pseudobulge-coherent* leads to similar results as the *pseudobulge-disk*, with a stronger preference for the *pseudobulge* model. This is consistent with the KS test results, which highlight the similarity between the *disk* and the *coherent* models, with the latter providing a slightly worse de-

scription of the data. We also tried to compare the odds ratio for different subsamples of galaxies within a given model. For example within the *pseudobulge* model we computed the odds ratio of accreting spirals over accreting ellipticals. The comparison yields $\log \Lambda \approx 8.4$, implying definitive evidence that the subsample of accreting ellipticals cannot provide a good description of the data. Analog results hold for all other galaxy subsamples.

4.4.2. Maximum likelihood: mixed models

Previous results favor the *pseudobulge* model; still this model provides a poor match to the clustering of spin measurements at $a_{bh} > 0.9$ seen in the data. It is therefore possible that a mix of the *pseudobulge* and *disk* model might provide a better description of the data. Based on this observation we constructed mixed models $M(\alpha)$ of the form

$$M(\alpha) = \alpha A + (1 - \alpha)B, \quad (25)$$

where α is a mixing parameter in the range $[0, 1]$. We take $A = \text{pseudobulge}$ and $B = \text{disk}$ and we compute the likelihood of the data given the model as a function of α according to equation (22), looking for the maximum. As a cross check, for each value of α we also compute the KS probability p_{KS} . Results are shown in table 5 and in the left panel of Figure 19 at different redshifts and under different assumptions of a_{bh} binning and observational error PDF. The α best matching the data is independent of redshift and error PDF assumptions, but depends on the number of a_{bh} bins, ranging from $\alpha \approx 0.55$ for 10 a_{bh} bins to $\alpha \approx 0.8$ for 30 a_{bh} . This is consistent with the fact that the *disk* model gets worse in describing the data as the number of bin increases, implying that its weight in a mixed model must decrease. By looking at Figure 19 we note, however, that the maximum is rather shallow, and the likelihood is rather flat in an α interval of width ≈ 0.5 around the maximum. This is because the data are sparse and not informative enough to select a specific value of mixing. The model yielding the maximum likelihood for 20 a_{bh} bins is shown in the right panel of Figure 19, where we see the good match with the data; the model can describe both the clustering at high spin values and the long-medium spin tail. We note, however, that in all cases shown in the left panel of Figure 19, the odds ratio between the best mixed model and the *pseudobulge* model is only ≈ 1 , making the former only marginally preferable.

5. DISCUSSION AND CONCLUSIONS

In this paper we presented the results of a semianalytical model for the evolution of galaxies and MBHs. The model keeps track (although in simplified ways) of the morphology of the galaxies, as well as the MBH masses and spins. For the first time we link the dynamical properties of the gas fueling the MBHs to the host galaxy properties, through different observationally based prescriptions. We stress that all the other similar investigations predicting MBH spin distributions either assumed “chaotic” accretion (MBHs accreting small gas clouds with isotropically oriented angular momenta) or “coherent” accretion (MBHs accreting all the time on a fixed plane).

Our model predicts different spin distributions for different types of galaxies. To date, only few MBH spins have been directly measured through $K\alpha$ iron line fitting (Reynolds 2013; Brenneman 2013). All the MBHs but one are hosted in low-redshift late type galaxies, preventing us from comparing our results for different galaxy types. We therefore tested

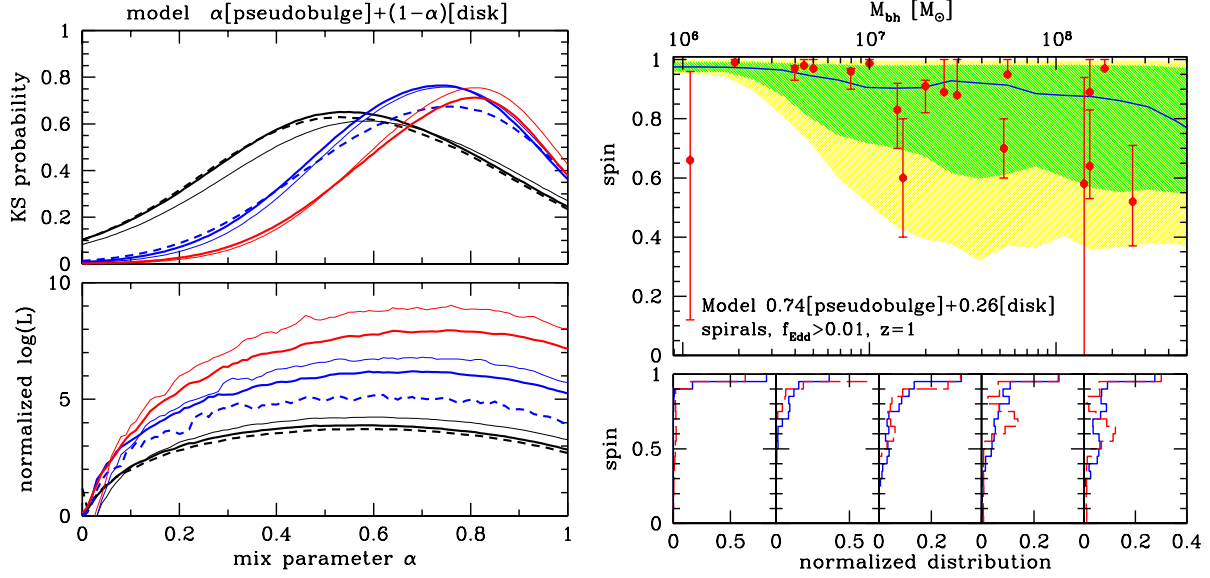


FIG. 19.— Mixed model analysis. The left plot show the KS probability (top panel) and the log likelihood (normalized to the value of the *disk* model, bottom panel) for the mixed model $\alpha[\text{pseudobulge}] + (1 - \alpha)[\text{disk}]$ as a function of the mixing parameter α . Colors are for different spin binning; 10 a_{bh} bins (black), 20 a_{bh} bins (blue) and 30 a_{bh} bins (red). For each color, thick solid and thin solid lines are computed considering model distributions at $z = 1$ and $z = 0.5$ respectively. The black dashed line is for 10 a_{bh} bins and flat errors in the spin measurements, and the blue dashed line is for 20 a_{bh} bins and a re-binning of the mass axis in 20 bins. The right plot shows a comparison of the model that best matches the observations when 20 a_{bh} bins are considered ($\alpha = 0.74$); line and color style are as in Figure 18.

our model by selecting low-redshift accreting MBHs hosted in spirals. For this galaxy class we have assumed three different gas dynamics prescriptions. In the *bulge* (*pseudobulge*) model we assumed that the dynamics of gas fueling the central MBHs is similar to that of the stars in galaxy bulges (*pseudobulges*). In the *disk* model, instead, the fueling gas has the more coherent dynamics of the large scale gas disk (see section 2.3 for details). For comparison, we have also run three separate sets of simulations adopting the standard coherent-accretion model, as well as two flavors of the chaotic-accretion model.

Our models produce interesting features in the MBH spin distribution, and a statistical comparison to observations yields a number of interesting results:

- i different galaxy morphologies result in different MBH spin distributions. Because the geometrical properties of the accretion flow are related to the large scale kinematics of the galaxy, MBHs hosted in ellipticals tend to have lower spins than those hosted in spirals;
- ii in general (with the exception of the *chaotic I* model), MBH spins are a decreasing function of the MBH mass: $\sim 10^6 M_{\odot}$ MBHs tend to be maximally spinning, whereas for masses $> 10^8 M_{\odot}$ a wide range of values is possible, depending on type of host and accretion rate of the MBH;
- iii accreting MBHs in spirals, i.e. those matching the observational sample, tend to spin fast, and *do not provide* an unbiased indicator of the underlying spin distribution of the overall MBH population;
- iv the *bulge* and *pseudobulge* models describe the observational data better than the *disk* one. The compatibility of the latter with the data strongly depends on the maximum value at which the MBH can be spun-up by accretion. If this value is $a_{\text{bh}} = 0.998$, then the *disk*

model can be safely ruled out at a $> 99\%$ confidence level, according to our 2D-KS tests;

- v a likelihood odds ratio study shows that the *pseudobulge* model: *i*) is strongly favored over the *disk* model even at the coarser a_{bh} binning; *ii*) is favored over the *bulge* one, but not at high significance;

- vi still, the best match with observations is given by a mix of the *pseudobulge* and *disk* model,. This indicates that there might be other factors, beyond the large scale galaxy morphology, influencing the geometry of the accretion flow;

- vii the simplistic *coherent*, *chaotic I* and *chaotic II* models provide a much poorer description of the data. The *coherent* model shows features similar to the *disk* model, but with a poorer agreement to the data; the chaotic models are unambiguously ruled out by observations.

We emphasize that the study of the evolution of the MBH spin distribution in a cosmological framework is still in its infancy. Because our model is idealized from many points of view, here we highlight some still-needed theoretical and observational improvements. *i*) The treatment of the Bardeen-Petterson effect, which plays a role in determining the fraction of prograde vs retrograde accretion events, is based on simple isotropic- α -viscosity driven accretion disks, and this assumption has been criticized by Sorathia et al. (2013b,a). The impact of this strong and debated assumption is unknown, since no working models of the MBH spin evolution relaxing it are available to date. *ii*) We assumed that every gas cloud fueling the MBHs weighs $M_{\text{cloud}} \sim 3 \times 10^4 M_{\odot}$. Giant molecular clouds are observed to have a broad mass spectrum. Observational studies of local galaxies reported typical molecular cloud mass functions with cut-offs at about $10^{5-6} M_{\odot}$ (e.g. Williams & McKee 1997; Engargiola et al. 2003; Fukui et al. 2008), making the average cloud mass of the order of the mass

we assumed. We note however that the cut-off mass seems to depend on the host galaxy properties (e.g. Hopkins 2012, and references therein). A simple implementation of a “characteristic” cloud mass function is not trivial, and beyond the scope of this paper. The effect of different average cloud masses can anyway be easily understood: the cloud mass contributes to setting the maximum MBH mass at which a complete alignment of the spin occurs at every accretion event, effectively making the fueling dynamics unimportant. At zeroth-order approximation (see Dotti et al. 2013, for a more detailed discussion) an order of magnitude variation of the average cloud mass results in an order of magnitude shift along the MBH mass axis of all the spin distributions. The results not showing any significant feature in the spin evolution (e.g. the *coherent*, *chaotic I*, and $f_{\text{Edd}} > 0.01$ *disk* models at low redshift) would remain mostly unchanged under a variation of the cloud masses. On the other hand, the *pseudobulge* model would predict higher spins for higher masses (lower spins for lower masses) if the cloud mass were higher (lower). We checked that a shift of one order of magnitude toward larger mass of the spin distributions does not affect the compatibility of the model with the data, yielding a KS probability > 0.3 . A similar shift of the distribution toward lower masses results in a slightly worse description of the data, but still with a KS probability of 0.1. *iii*) Our dynamical prescriptions for the nuclear gas dynamics are mostly based on gas and/or stellar dynamics observations on scales much larger than the accretion disk or the MBH sphere of influence. Our model would greatly benefit from a description of the gas dynamics on scales $\lesssim 100$ pc, already achievable in some cases with high resolution ALMA spectroscopy (e.g. Combes et al. 2013, 2014). Finally, *iv*) in our model we completely neglected the effect of rotational energy extraction from the MBH and its effect on the spin. This could in principle power relativistic jets through the Blandford-Znajek mechanism, limiting the maximum spin to lower values in radio galaxies.

From an observational point of view, the main improvement would consist in enlarging the currently small sample of measured MBH spins, and to extend it to higher redshift and different galaxy types. In this regard, the forthcoming Astro-H satellite will have exquisite combined spectral resolution and sensitivity, making $K\alpha$ -based spin measurements possible perhaps up to $z \sim 1$ (Takahashi et al. 2012). Along the same lines, Athena+, to be launched in 2028, will push such measurements to $z \sim 2$ for extremely X-ray bright systems, significantly expanding the observed spin sample (Dovciak et al. 2013). On a shorter timescale, the eROSITA satellite will observe $> 10^5$ AGNs. Image stacking in luminosity and redshift bins will reveal the ‘average’ shape of the $K\alpha$ line of these systems, making possible to study trends in the typical spin of AGNs across a large mass range and for redshifts perhaps up to $z \sim 1$ (Merloni et al. 2012), providing an important benchmark for comparison to theoretical models. On a different note, the eLISA mission, now selected by ESA for the L3 launch slot, will measure the spins of merging MBH binaries across the cosmic history to high precision, providing a sample that will not be biased toward high X-ray luminosities.

Even though the future of spin measurements looks literally bright, we should also keep in mind that the uncertainties on the value of measured spins depend on the technique used. Different methods have been used to constrain the MBH spin distribution at different redshifts and for different masses. Some methods estimate the spin value from the radio proper-

ties of the AGNs (e.g. Daly & Sprinkle 2013, and references therein), from the ionizing flux required to produce the observed broad emission lines (Netzer & Trakhtenbrot 2013), or fitting the continuum from the accretion disk (Davis & Laor 2011). Some of these methods are still matter of debate (e.g. Gallo et al. 2012; Raimundo et al. 2012; Laor & Davis 2011), and all of them require an independent measure of the MBH mass to estimate its spin. In this paper we compared our predictions with the mass independent measurements obtained through relativistically broadened iron $K\alpha$ line fitting, to prevent any possible spurious mass spin correlation. We refer to Reynolds (2013) and Brenneman (2013) for a detailed discussion of the uncertainties on these measurements. Since we find a significant evolution of the MBH spins as a function of their masses, the uncertainties on the MBH masses are fundamental as well. For example, one Mrk 359, has an estimated mass of $\approx 10^6 M_\odot$, obtained through a single epoch measurement of the continuum and broad $H\beta$ FWHM (Zhou & Wang 2005). The width of the line is only 480 km s^{-1} significantly smaller than the typical value for type 1 AGN as well as than the threshold for being classified as a NLS1. Since the MBH is hosted in a spiral galaxy the line is peculiarly large to be associated with a single narrow line, and a broad component is expected because of the point like emission clearly visible in the HST imaging (Malkan et al. 1998). The observed line width could be so narrow because of orientation effects, already suggested to be significant for NLS1s (Decarli et al. 2008), causing an underestimation of the MBH mass¹³. More independent measurements of the masses of MBHs with spin estimates would help in better constraining their values. The detection of gravitational waves will greatly improve the situation, giving high precision measures of the MBH masses and spins, that could be compared with predictions for merging systems.

Regardless the large uncertainties we commented on above, it is remarkable that two of the models (*bulge* and *pseudobulge*) that we investigated generate sets of MBH masses and spins consistent with the observations. Since these models assume that the gas has a less coherent dynamics than the larger-scale gas structure, our analysis seems to suggest the existence of a physical process that, while decreasing the gas angular momentum magnitude (triggering accretion in the first place), reshuffles the gas angular momentum direction as well. Such a reshuffling could be caused by local processes, i.e. star formation and the torques exerted by the gas self-gravity (e.g. Maio et al. 2013), as well as larger scales gravitational instabilities and violent gas inflows (e.g. Hopkins et al. 2012; Dubois et al. 2014). In any case, in order to have such a good agreement between the predictions of the model and the observed spins, we require the accreting gas to have, on average, a non-zero angular momentum, i.e. the gas must *not* accrete isotropically onto the MBH. We have in fact shown that a perfectly isotropic accretion flow would result in significantly slower spinning MBHs for intermediate to large MBH masses, which is inconsistent with observations.

We further note that a mix of the *pseudobulge* and *disk* model provides the best description of the data. This might imply that the reshuffling mentioned above may be only partial, and its efficiency might depend on other factors, thus allowing the gas inflow to be more or less ‘coherent’ under dif-

¹³ We checked that the contribution of Mrk 359 to our analysis is negligible. Its MBH spin is so poorly constrained that removing it from the observational sample has no effect on our results.

ferent circumstances. The currently available spin data seem to agree with a simple evolutionary model for disk galaxies, which we sketch in the following. Pseudobulges have recently been associated with stellar bars, i.e., structures able to drive gas inflows toward the galaxy nuclei (see, e.g. Sellwood 2013; Kormendy 2013, for up to date reviews). After the initial instability responsible for the bar formation, the bar itself generally undergoes a thickening that can be either caused by a second “buckling” instability or by a vertical resonance (see Sellwood 2013, for a more detailed discussion), possibly responsible for the pseudobulge formation (see Kormendy 2013, for an extensive and updated review). In this scenario, the gas could accrete with a more disk like dynamics until the bar thickens, and fall toward the MBH with a higher velocity dispersion after the pseudobulge forms if the buckling instability and/or any vertical resonance significantly affect the gas motion too. The construction of a formal dynamical model for this process is beyond the scope of this paper. Still, if the statistical (not very significant, at this point) preference

of the pseudobulge-disk composite model will be confirmed by more data, it could point toward a physically motivated galaxy-MBH coevolution scenario for low redshift disk galaxies, in which the dynamics of gas in nuclear bars drives the MBH mass and spin evolution.

We thank M. Colpi, D. Calzetti, J. Gair, M. Kesden, M. R. Krumholz, A. Merloni, C. Reynolds, A. Tchekhovskoy and M. Volonteri for insightful comments and discussions. We acknowledge support from the European Unions Seventh Framework Program (FP7/PEOPLE-2011-CIG) through the Marie Curie Career Integration Grant GALFORMbHS PCIG11-GA-2012-321608 (to E.B.), and support from the DLR (Deutsches Zentrum für Luft- und Raumfahrt) through the DFG grant SFB/TR 7 Gravitational Wave Astronomy and (to A.S.). Computations were performed on the gpc supercomputer at the SciNet HPC Consortium, as well as on the “Projet Horizon Cluster” at the Institut d’astrophysique de Paris.

REFERENCES

- Barausse, E. 2012, *MNRAS*, 423, 2533
 Barausse, E., Morozova, V., & Rezzolla, L. 2012, *ApJ*, 758, 63
 Barausse, E., & Rezzolla, L. 2009, *ApJ*, 704, L40
 Barausse, E., & Sotiriou, T. P. 2013, *Classical and Quantum Gravity*, 30, 244010
 Bardeen, J. M., & Petterson, J. A. 1975, *ApJ*, 195, L65
 Begelman, M. C., Blandford, R. D., & Rees, M. J. 1980, *Nature*, 287, 307
 Bernardi, M., Meert, A., Sheth, R. K., et al. 2013, *MNRAS*, 436, 697
 Bernardi, M., Shankar, F., Hyde, J. B., et al. 2010, *MNRAS*, 404, 2087
 Berti, E., & Volonteri, M. 2008, *ApJ*, 684, 822
 Bigiel, F., Leroy, A., Walter, F., et al. 2010, *AJ*, 140, 1194
 Blandford, R. D., & McKee, C. F. 1982, *ApJ*, 255, 419
 Blandford, R. D., & Znajek, R. L. 1977, *MNRAS*, 179, 433
 Bolatto, A. D., Leroy, A. K., Jameson, K., et al. 2011, *ApJ*, 741, 12
 Bower, R. G., Benson, A. J., Malbon, R., et al. 2006, *MNRAS*, 370, 645
 Brenneman, L. 2013, *Measuring the Angular Momentum of Supermassive Black Holes*, doi:10.1007/978-1-4614-7771-6
 Broderick, A. E., Loeb, A., & Narayan, R. 2009, *ApJ*, 701, 1357
 Broderick, A. E., & Narayan, R. 2006, *ApJ*, 638, L21
 Buonanno, A., Kidder, L. E., & Lehner, L. 2008, *Phys. Rev. D*, 77, 026004
 Calderone, G., Ghisellini, G., Colpi, M., & Dotti, M. 2013, *MNRAS*, 431, 210
 Cappellari, M., Emsellem, E., Bacon, R., et al. 2007, *MNRAS*, 379, 418
 Castignani, G., Haardt, F., Lapi, A., et al. 2013, *ArXiv e-prints*, arXiv:1309.4108
 Cole, S., Helly, J., Frenk, C. S., & Parkinson, H. 2008, *MNRAS*, 383, 546
 Combes, F., García-Burillo, S., Casasola, V., et al. 2013, *A&A*, 558, A124
 Combes, F., García-Burillo, S., Casasola, V., et al. 2014, *ArXiv e-prints*, arXiv:1401.4120
 Conselice, C. J. 2006, *MNRAS*, 373, 1389
 Consortium, T. e., Seoane, P. A., et al. 2013, *ArXiv e-prints*, arXiv:1305.5720
 Croton, D. J., Springel, V., White, S. D. M., et al. 2006, *MNRAS*, 365, 11
 Daddi, E., Elbaz, D., Walter, F., et al. 2010, *ApJ*, 714, L118
 Daly, R. A., & Sprinkle, T. B. 2013, *ArXiv e-prints*, arXiv:1312.4862
 Davis, S. W., & Laor, A. 2011, *ApJ*, 728, 98
 De Lucia, G., & Blaizot, J. 2007, *MNRAS*, 375, 2
 Decarli, R., Dotti, M., Fontana, M., & Haardt, F. 2008, *MNRAS*, 386, L15
 Dotti, M., Colpi, M., Pallini, S., Perego, A., & Volonteri, M. 2013, *ApJ*, 762, 68
 Dotti, M., Volonteri, M., Perego, A., et al. 2010, *MNRAS*, 402, 682
 Dovciak, M., Matt, G., Bianchi, S., et al. 2013, *ArXiv e-prints*, arXiv:1306.2331
 Dubois, Y., Volonteri, M., & Silk, J. 2013, *ArXiv e-prints*, arXiv:1304.4583
 Dubois, Y., Volonteri, M., Silk, J., Devriendt, J., & Slyz, A. 2014, *ArXiv e-prints*, arXiv:1401.1220
 Elbaz, D., & Cesarsky, C. J. 2003, *Science*, 300, 270
 Engargiola, G., Plambeck, R. L., Rosolowsky, E., & Blitz, L. 2003, *ApJS*, 149, 343
 Epinat, B., Tasca, L., Amram, P., et al. 2012, *A&A*, 539, A92
 Fabricius, M. H., Saglia, R. P., Fisher, D. B., et al. 2012, *ApJ*, 754, 67
 Fanidakis, N., Baugh, C. M., Benson, A. J., et al. 2011, *MNRAS*, 410, 53
 —. 2012, *MNRAS*, 419, 2797
 Ferrarese, L., & Merritt, D. 2000, *ApJ*, 539, L9
 Forbes, J. C., Krumholz, M. R., Burkert, A., & Dekel, A. 2013, *ArXiv e-prints*, arXiv:1311.1509
 Förster Schreiber, N. M., Genzel, R., Bouché, N., et al. 2009, *ApJ*, 706, 1364
 Fukui, Y., Kawamura, A., Minamidani, T., et al. 2008, *ApJS*, 178, 56
 Gair, J. R., Tang, C., & Volonteri, M. 2010, *Phys. Rev. D*, 81, 104014
 Gallo, E., Russell, D., & Fender, R. 2012, in *Half a Century of X-ray Astronomy*, Proceedings of the conference held 17-21 September, 2012 in Mykonos Island, Greece.
 Gammie, C. F., Shapiro, S. L., & McKinney, J. C. 2004, *ApJ*, 602, 312
 Gebhardt, K., Bender, R., Bower, G., et al. 2000, *ApJ*, 539, L13
 Genzel, R., Tacconi, L. J., Gracia-Carpio, J., et al. 2010, *MNRAS*, 407, 2091
 Ghez, A. M., Salim, S., Weinberg, N. N., et al. 2008, *ApJ*, 689, 1044
 Gibbons, G. 1975, *Commun.Math.Phys.*, 44, 245
 Gillessen, S., Eisenhauer, F., Trippe, S., et al. 2009, *ApJ*, 692, 1075
 Gnerucci, A., Marconi, A., Cresci, G., et al. 2011, *A&A*, 528, A88
 Goldreich, P., & Julian, W. H. 1969, *ApJ*, 157, 869
 Granato, G. L. private communication
 Granato, G. L., De Zotti, G., Silva, L., Bressan, A., & Danese, L. 2004, *ApJ*, 600, 580
 Gültekin, K., Richstone, D. O., Gebhardt, K., et al. 2009, *ApJ*, 698, 198
 Guo, Q., White, S., Boylan-Kolchin, M., et al. 2011, *MNRAS*, 413, 101
 Haiman, Z., Ciotti, L., & Ostriker, J. P. 2004, *ApJ*, 606, 763
 Hanni, R. S. 1982, *Phys.Rev.D*, 25, 2509
 Häring, N., & Rix, H.-W. 2004a, *ApJ*, 604, L89
 —. 2004b, *ApJ*, 604, L89
 Heckman, T. M., Kauffmann, G., Brinchmann, J., et al. 2004, *ApJ*, 613, 109
 Hickox, R. C., Jones, C., Forman, W. R., et al. 2009, *ApJ*, 696, 891
 Hicks, E. K. S., & Malkan, M. A. 2008, *ApJS*, 174, 31
 Hopkins, P. F. 2012, *MNRAS*, 423, 2016
 Hopkins, P. F., Hernquist, L., Hayward, C. C., & Narayanan, D. 2012, *MNRAS*, 425, 1121
 Hopkins, P. F., Richards, G. T., & Hernquist, L. 2007, *ApJ*, 654, 731
 Kaspi, S., Maoz, D., Netzer, H., et al. 2005, *ApJ*, 629, 61
 Kassian, S. A., Weiner, B. J., Faber, S. M., et al. 2012, *ApJ*, 758, 106
 Kauffmann, G., & Heckman, T. M. 2009, *MNRAS*, 397, 135
 Kerr, R. P. 1963, *Phys.Rev.Lett.*, 11, 237
 Khandai, N., Di Matteo, T., Croft, R., et al. 2014, *ArXiv e-prints*, arXiv:1402.0888
 King, A. R., Lubow, S. H., Ogilvie, G. I., & Pringle, J. E. 2005, *MNRAS*, 363, 49
 King, A. R., & Pringle, J. E. 2006, *MNRAS*, 373, L90
 Kormendy, J. 2013, *ArXiv e-prints*, arXiv:1311.2609
 Kormendy, J., & Richstone, D. 1995, *ARA&A*, 33, 581
 Krumholz, M. R. 2012, *ApJ*, 759, 9
 Krumholz, M. R., & Gnedin, N. Y. 2011, *ApJ*, 729, 36
 Krumholz, M. R., & McKee, C. F. 2005, *ApJ*, 630, 250

- Krumholz, M. R., McKee, C. F., & Tumlinson, J. 2009, *ApJ*, 699, 850
- Kuhlen, M., Madau, P., & Krumholz, M. R. 2013, *ApJ*, 776, 34
- Lagos, C. D. P., Padilla, N. D., & Cora, S. A. 2009, *MNRAS*, 395, 625
- Laor, A., & Davis, S. 2011, *ArXiv e-prints*, arXiv:1110.0653
- Law, D. R., Steidel, C. C., Erb, D. K., et al. 2009, *ApJ*, 697, 2057
- Lousto, C. O., & Zlochower, Y. 2009, *Phys. Rev. D*, 79, 064018
- Lusso, E., Comastri, A., Simmons, B. D., et al. 2012, *MNRAS*, 425, 623
- Magorrian, J., Tremaine, S., Richstone, D., et al. 1998, *AJ*, 115, 2285
- Maio, U., Dotti, M., Petkova, M., Perego, A., & Volonteri, M. 2013, *ApJ*, 767, 37
- Maoz, E. 1998, *ApJ*, 494, L181
- Marconi, A., & Hunt, L. K. 2003, *ApJ*, 589, L21
- McConnell, N. J., & Ma, C.-P. 2013, *ApJ*, 764, 184
- Merloni, A., Rudnick, G., & Di Matteo, T. 2004, *MNRAS*, 354, L37
- Merloni, A., Predehl, P., Becker, W., et al. 2012, *ArXiv e-prints*, arXiv:1209.3114
- Miyoshi, M., Moran, J., Herrnstein, J., et al. 1995, *Nature*, 373, 127
- Nandra, K., Barret, D., Barcons, X., et al. 2013, *ArXiv e-prints*, arXiv:1306.2307
- Narayan, R., McClintock, J. E., & Tchekhovskoy, A. 2013, *ArXiv e-prints*, arXiv:1303.3004
- Netzer, H., & Trakhtenbrot, B. 2013, *MNRAS*, arXiv:1311.4215
- Newman, E. T., Couch, E., Chinnappared, K., et al. 1965, *Journal of Mathematical Physics*, 6, 918
- Newman, S. F., Genzel, R., Förster Schreiber, N. M., et al. 2013, *ApJ*, 767, 104
- Pani, P., & Cardoso, V. 2009, *Phys.Rev.*, D79, 084031
- Pani, P., Macedo, C. F., Crispino, L. C., & Cardoso, V. 2011, *Phys.Rev.*, D84, 087501
- Perego, A., Dotti, M., Colpi, M., & Volonteri, M. 2009, *MNRAS*, 399, 2249
- Press, W. H., Teukolsky, S. A., Vetterling, W. T., & Flannery, B. P. 1992, *Numerical recipes in FORTRAN. The art of scientific computing*
- Raimundo, S. I., Fabian, A. C., Vasudevan, R. V., Gandhi, P., & Wu, J. 2012, *MNRAS*, 419, 2529
- Reynolds, C. S. 2013, *ArXiv e-prints*, arXiv:1307.3246
- Rezzolla, L., Barausse, E., Dorband, E. N., et al. 2008, *Phys. Rev. D*, 78, 044002
- Risaliti, G., Harrison, F. A., Madsen, K. K., et al. 2013, *Nature*, 494, 449
- Ruderman, M. A., & Sutherland, P. G. 1975, *ApJ*, 196, 51
- Scannapieco, E., Silk, J., & Bouwens, R. 2005, *ApJ*, 635, L13
- Schödel, R., Ott, T., Genzel, R., et al. 2002, *Nature*, 419, 694
- Sellwood, J. A. 2013, *ArXiv e-prints*, arXiv:1310.0403
- Sesana, A., Gair, J., Berti, E., & Volonteri, M. 2011, *Phys. Rev. D*, 83, 044036
- Shankar, F. 2013, *Classical and Quantum Gravity*, 30, 244001
- Shankar, F., Salucci, P., Granato, G. L., De Zotti, G., & Danese, L. 2004, *MNRAS*, 354, 1020
- Shankar, F., Weinberg, D. H., & Miralda-Escudé, J. 2009, *ApJ*, 690, 20
- Soltan, A. 1982, *MNRAS*, 200, 115
- Sorathia, K. A., Krolik, J. H., & Hawley, J. F. 2013a, *ApJ*, 777, 21
- . 2013b, *ApJ*, 768, 133
- Swinbank, A. M., Sobral, D., Smail, I., et al. 2012, *MNRAS*, 426, 935
- Takahashi, T., Mitsuda, K., Kelley, R., et al. 2012, in *Society of Photo-Optical Instrumentation Engineers (SPIE) Conference Series*, Vol. 8443, *Society of Photo-Optical Instrumentation Engineers (SPIE) Conference Series*
- Tchekhovskoy, A., Narayan, R., & McKinney, J. C. 2010, *ApJ*, 711, 50
- Thorne, K. S. 1974, *ApJ*, 191, 507
- van Meter, J. R., Miller, M. C., Baker, J. G., Boggs, W. D., & Kelly, B. J. 2010, *ApJ*, 719, 1427
- Volonteri, M., Madau, P., Quataert, E., & Rees, M. J. 2005, *ApJ*, 620, 69
- Volonteri, M., Sikora, M., & Lasota, J.-P. 2007, *ApJ*, 667, 704
- Volonteri, M., Sikora, M., Lasota, J.-P., & Merloni, A. 2013, *ApJ*, 775, 94
- Wilkins, S. M., Trentham, N., & Hopkins, A. M. 2008, *MNRAS*, 385, 687
- Williams, J. P., & McKee, C. F. 1997, *ApJ*, 476, 166
- Wisnioski, E., Glazebrook, K., Blake, C., et al. 2011, *MNRAS*, 417, 2601
- Yagi, K., Yunes, N., & Tanaka, T. 2012, *Phys.Rev.*, D86, 044037